POLITECNICO DI TORINO
Repository ISTITUZIONALE

A Comparative Study of the DEKF and DUKF for Battery SOC and SOH Estimation

Original
A Comparative Study of the DEKF and DUKF for Battery SOC and SOH Estimation / Seifoddini, A., Miretti, F., Misul, D.A.. - In: BATTERIES. - ISSN 2313-0105. - ELETTRONICO. - (2025). [10.3390/batteries11110410]

Availability:
This version is available at: 11583/3004935 since: 2025-11-07T07:59:03Z

Publisher:
MDPI

Published
DOI:10.3390/batteries11110410

Terms of use:

This article is made available under terms and conditions as specified in the corresponding bibliographic description in the repository

Publisher copyright

(Article begins on next page)

31 October 2026

batteries

MDPI

Article

A Comparative Study of the DEKF and DUKF for Battery SOC and SOH Estimation

Arash Seifoddini, Federico Miretti * and Daniela Anna Misul *

Department of Energy (DENERG) and Center for Automotive Research and Sustainable Mobility (CARS@Polito), Politecnico di Torino, Corso Duca degli Abruzzi 24, 10129 Torino, TO, Italy; arash.seifoddini@studenti.polito.it
* Correspondence: federico.miretti@polito.it (F.M.); daniela.misul@polito.it (D.A.M.)

Abstract

The accurate estimation of the state of charge (SOC) and state of health (SOH) is essential for the safety and reliability of electric vehicle batteries. Conventional single-state Kalman filters are prone to parameter drift caused by cell aging, which leads to persistent SOC estimation errors. This study compares two dual-estimator methods, the Dual Extended Kalman Filter (DEKF) and the Dual Unscented Kalman Filter (DUKF), for simultaneous SOC and SOH estimation using a second-order equivalent-circuit model. The process and measurement covariance matrices were tuned through a structured optimization procedure to ensure consistent performance under different drive cycles and initialization errors. To mitigate the weak voltage sensitivity to capacity, synthetic SOC–capacity coupling was introduced to enhance SOH observability and accelerate convergence. Simulations conducted under the Urban Dynamometer Driving Schedule (UDDS) and a real-world CLUST7 profile demonstrated SOC root-mean-square errors near 2% for both filters. The DUKF achieved faster and smoother convergence than the DEKF but required roughly fivefold higher computational cost. These findings provide quantitative evidence supporting dual Kalman filtering as an effective framework for accurate and robust SOC/SOH estimation in production battery management systems.

Keywords: state of charge; state of health; electric vehicle batteries; dual Kalman filter; extended Kalman filter; unscented Kalman filter; battery management system

check for updates

Academic Editors: Truong Minh Ngoc Bui, Truong Quang Dinh and Mona Faraji Niri

Received: 29 September 2025
Revised: 28 October 2025
Accepted: 3 November 2025
Published: 5 November 2025

Citation: Seifoddini, A.; Miretti, F.; Misul, D.A. A Comparative Study of the DEKF and DUKF for Battery SOC and SOH Estimation. *Batteries* **2025**, *11*, 410. https://doi.org/10.3390/batteries11110410

Copyright: © 2025 by the authors. Licensee MDPI, Basel, Switzerland. This article is an open access article distributed under the terms and conditions of the Creative Commons Attribution (CC BY) license (https://creativecommons.org/licenses/by/4.0/).

1. Introduction

Accurate knowledge of a battery's *state of charge* (SOC) and *state of health* (SOH) is essential for the safe and efficient operation of battery-electric vehicles (BEVs). Reliable SOC estimates prevent unexpected range loss and limit over-charge or over-discharge events, while accurate SOH tracking enables aging-aware power limits and service life predictions. These quantities are not directly measurable and must be derived from voltage, current, and temperature data using estimation algorithms [1–3], and various methodologies have been developed to solve this underlying problem [4–7].

Early battery management systems (BMSs) relied on *feature-based* techniques such as Coulomb counting and open-circuit voltage (OCV) reference curves. Although substantial work has been conducted to improve these approaches [8–11], they remain impractical as standalone solutions, as they are vulnerable to sensor bias and noise accumulation, unknown initial SOC estimate, temperature dependence, OCV hysteresis, and aging-induced OCV drift. Moreover, OCV curves are relatively flat over wide SOC ranges, which

limits observability under typical drive cycles. These limitations motivate methods that fuse models with sensor measurements to maintain accuracy in real-world operating conditions.

More recently, *data-driven* methods that range from classical machine learning (e.g., support vector regression, Gaussian processes) to deep learning architectures have been explored to map measured signals to SOC/SOH directly [12–18]. These approaches can capture strong nonlinearities and implicit aging effects when trained on representative datasets, and they often deliver high accuracy in controlled test scenarios. Hybrid approaches combining equivalent-circuit models (ECMs) with data-driven algorithms have also been investigated for SOH estimation. Chen et al. [19] integrated a first-order ECM with a neural network, where internal resistance identified via particle swarm optimization was used as an input feature, achieving an SOH RMSE below 1.35%. Yang et al. [20] estimated the ECM aging parameter using a Kalman filter and applied regression analysis to select resistance-related indicators, which were then used by a long short-term memory network for SOH prediction. Similarly, Lyu et al. [21] combined an ECM with a linear regression model to form a state-space representation of capacity degradation, enabling Kalman-filter-based SOH tracking. Beyond lithium-ion chemistries, recent studies have introduced hybrid frameworks combining physics-based models and machine learning for SOC and SOH estimation across diverse systems such as Ni–Zn, Na-ion, and Li-ion batteries [22]. These approaches emphasize data-driven reliability prediction and sensor-assisted monitoring, complementing the model-based dual Kalman filter methods evaluated in this study.

Nonetheless, practical deployment in production is challenging due to the need for large, well-labeled datasets and their high computation and memory costs for embedded automotive hardware. These constraints motivate the continued adoption of *model-based* approaches, particularly Kalman-filter-based variants, that fuse estimates from a battery model with noisy sensor measurements in production BMSs.

These techniques typically rely on a physics-inspired *equivalent-circuit model* (ECM), such as the second-order resistance–capacitance (RC) ECM, as it offers a good balance between model fidelity and computational cost [3,23]. Historically, *single-estimator* Kalman filters such as the *extended* (EKF) and *unscented* filters (UKF) were deployed to track the fast-changing SOC state in real time. The EKF linearizes the nonlinear ECM around the latest estimate, with Plett [24] establishing an EKF-based framework for SOC estimation. Building on this, He et al. [25] proposed an adaptive EKF (AEKF) using an improved Thevenin model with an extra RC branch, achieving lower max and mean SOC errors under different urban drive cycles, while He et al. [26] performed online parameter and SOC estimation for $LiFePO_4$ cells. In addition, Ramadan et al. [27] integrated the effect of hysteresis on an OCV-SOC map and demonstrated EKF feasibility on microcontrollers. For UKF-type methods, Plett [28] introduced the sigma-point Kalman filter approach for SOC estimation, which resulted in accuracy gains at higher computational costs. Sun et al. [29] developed an adaptive UKF with covariance matching that outperformed EKF/UKF/AEKF baselines in accuracy, and Tian et al. [30] coupled the UKF with a modified ECM whose resistance and capacity depended on rate, SOC, and temperature, using lookup-table corrections to reduce computational load while improving accuracy. Together, these EKF/UKF developments demonstrated strong real-time SOC performance but also revealed sensitivity to aging-driven parameter drift.

To resolve the parameter drift problem, *dual-estimator* Kalman filter architectures split estimation into a fast *state filter* (SOC and RC voltages) and a slow *parameter filter* (capacity, resistances). Plett [28] established a foundation model for dual-estimator schemes. Wassiliadis et al. [31] performed a life-cycle analysis with numerically optimized filter parameters and confirmed the DEKF's SOC advantage over a single EKF across aging while

highlighting unreliable and divergent capacity and resistance estimates under constant loads and advanced degradation. Ref. [32] investigated computationally efficient structures for SOC/SOH estimation, investigating the coupling between model fidelity and estimator robustness. Ref. [33] developed a dual filter that coupled a standard KF and a UKF that achieved sub-1% SOC error and accurate resistance tracking across aging tests. Wang et al. [34] introduced a dual UKF (DUKF) that achieved online parameter identification and SOC estimation with <3% maximum SOC error across operating conditions. Kim et al. [35] deployed a pattern-aided DEKF using a Hamming neural network, which selected representative voltage and capacity patterns to transfer model parameters without repeated identification, improving SOC/capacity estimation. Fang et al. [36] demonstrated that a DEKF combined with forgetting-factor RLS provided accurate online parameter identification and joint SOC/SOH estimation and noted that the OCV–SOC curve dominated the SOC/SOH error sensitivity.

While many studies have analyzed different variants of *single* and *dual* Kalman filters, the SOH remains difficult to observe due to the low sensitivity of the terminal voltage to capacity changes within nominal operating windows [3,37]. Additionally, reported conclusions are often hindered by inconsistent covariance tuning and constrained test conditions. This study addresses these limitations by performing the following: (i) stabilizing UKF/DUKF convergence with two enhancements, which improve DUKF estimation performance substantially; (ii) tuning covariance matrices via a structured, log-space optimization technique that mitigates overfitting and delivers suitable performance across diverse driving profiles and cell age scenarios; and (iii) conducting a thorough comparison across distinct drive cycles and controlled grids of initial SOC and capacity errors using a common model based on shared metrics. Collectively, these elements provide a fair head-to-head assessment of the DEKF versus DUKF methodologies and practical guidance for BMS deployment.

Both filters share the same second-order ECM and are evaluated on high-resolution laboratory data under the Urban Dynamometer Driving Schedule (UDDS) and a real-world drive cycle.

The main contributions are as follows:

- A MATLAB/Simulink framework that enables the repeatable benchmarking of dual Kalman filters under identical numerical settings.
- A comprehensive comparison of SOC and SOH accuracy, convergence speed, bias sensitivity, and computational load.
- Practical tuning guidelines for the Kalman filter covariance matrices.

2. Methodology

This chapter outlines the modeling, estimation, and validation procedures used in this study to compare the performance of DEKF and DUKF-based Kalman filters for the state and parameter estimation of lithium-ion batteries. The methodology consists of three main components: (i) a physics-inspired ECM that captures the battery's electrical dynamics, (ii) Kalman filter variants to estimate both fast-varying states and slowly drifting aging parameters, and (iii) a repeatable evaluation framework built in MATLAB/Simulink to assess estimation accuracy, robustness, and computational cost.

First, Section 2.1 describes the source of the test data and the ECM formulation, including discretizations and parameter definitions. Then, Section 2.2 details the structure and configuration of each estimator, including the coupling scheme used in the dual filters. Finally, implementation aspects such as solver settings and runtime settings are discussed to support reproducibility and ensure a side-by-side comparison.

2.1. Battery Cell and Driving Cycle Simulation Data

This study uses the publicly available dataset described in [38], which contains experimental measurements from ten NMC cells (the INR21700-M50T cells manufactured by LG Chem) over a 30-month aging campaign. The cycling protocol aimed to reproduce aging conditions similar to those experienced in electric vehicles (EVs), using the Urban Dynamometer Driving Schedule (UDDS) for the driving phases. The UDDS is repeated until the SOC drops to 20%, after which the cell is charged with a CC-CV protocol.

To augment the dataset originally obtained with the UDDS drive cycle, synthetic data were generated using the electrochemical cell model developed by [39] to represent an additional driving cycle, denoted here as CLUST7. Since standardized drive cycles, while reproducible, often fail to capture the variability in real-world conditions for electrified vehicles [40], the CLUST7 experimental cycle was included. This cycle was recorded under real driving conditions and is described in Section 3.1.3. Current profiles were obtained with a vehicle simulation model starting from the drive cycle; then, the terminal voltage data were generated using the electrochemical model using the current profiles as input. The simulation was repeated for a number of cycles in order to achieve a discharge from 80% to 20% SOC.

Although the INR21700-M50T cell (an NMC cell) was selected for this study, the adopted second-order ECM and dual Kalman filter structures are chemistry-agnostic. When applied to other chemistries such as LFP, only the model parameters (e.g., OCV–SOC curve, resistances, and capacity) require re-identification, while the estimation framework remains unchanged.

2.2. Simulation Model

The model is utilized in a model-in-the-loop (MIL) framework with the following key components:

- **Battery model**: The ECM, which can be implemented as either a Simulink model or a MATLAB script.
- **Uncertainty characterization**: Process and measurement disturbances are treated as mutually uncorrelated, zero-mean, white Gaussian sequences, consistent with standard Kalman filter assumptions [41].
- **Drive cycle emulation**: Terminal current $i(t)$ is drawn from UDDS, CLUST17, and highway profiles to simulate the full dynamic range.

The foundation of effective battery state estimation relies on creating an accurate yet computationally efficient model that closely mirrors battery behavior. Deriving an exact electrochemical representation of lithium-ion batteries (LIBs) is impractical for typical automotive BMSs due to their limited computational resources and the inherent complexity of battery operation. To address this challenge, researchers commonly utilize ECMs, which simplify the battery processes into manageable electrical circuit representations. In this study, cell dynamics are represented by a second-order RC equivalent-circuit model, which is widely used in the literature due to its acceptable trade-off between model fidelity and computational burden [23–25,42].

The ECM topology used in this study is shown in Figure 1 and comprises the following:

- **Open-Circuit Voltage (OCV) Source,** $U_{\mathrm{OCV}}(\mathrm{SOC})$: This represents the equilibrium terminal voltage of the battery as a function of its SOC, and it reflects the cell's internal electrochemical potential.
- **Ohmic Terminal Resistance,** R_0: This models instantaneous voltage drop due to internal resistive losses in the cell, including electrode interfaces, electrolyte resistance, and current collectors.

- **Two RC Branches,** (R_1, C_1) and (R_2, C_2): These components model the dynamic behavior of the battery. The first RC pair captures short-term transient voltage drops (e.g., double-layer capacitance and charge transfer), while the second models longer time-constant diffusion effects [31].
- **Total Capacity,** (C_p): A slowly varying capacity that tracks aging-induced fade [43].

The current $i(t)$ enters the circuit at the positive terminal, flows through R_0, then splits into the two RC networks, and finally charges the equivalent capacitor that defines the SOC.

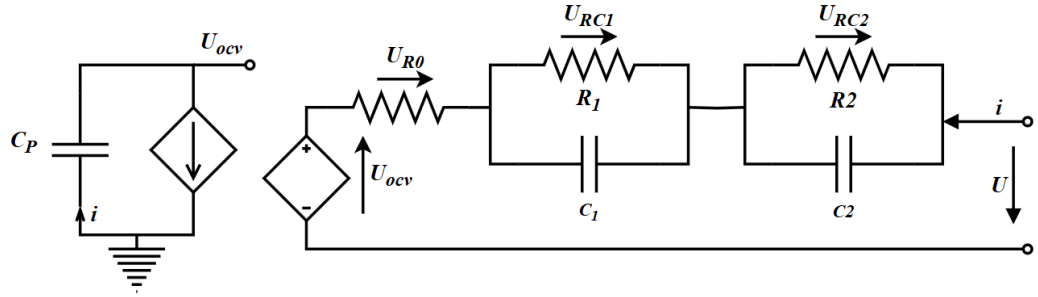


Figure 1. Second-order ECM with open-circuit voltage, ohmic resistance R_0, total capacity C_p, and two RC branches representing dynamic polarization and diffusion.

2.3. Discrete State-Space Representation

The ECM is formulated as a discrete-time state-space model to enable observer design. With the sampling interval Δt, the ECM is expressed as follows:

$$\mathbf{x}_k = \mathbf{f}(\mathbf{x}_{k-1}, \mathbf{u}_{k-1}) + \mathbf{w}_{k-1} \qquad \mathbf{w}_{k-1} \sim \mathcal{N}(\mathbf{0}, \mathbf{Q}_{k-1}) \tag{1a}$$

$$\mathbf{y}_k = \mathbf{g}(\mathbf{x}_k, \mathbf{u}_k) + \mathbf{v}_k \qquad \mathbf{v}_k \sim \mathcal{N}(\mathbf{0}, \mathbf{R}_k) \tag{1b}$$

where $u_k = i_k$ is the measured terminal current; $y_k = U_k$ is the measured terminal voltage; w_k and v_k represent process and measurement noise, respectively; and $\mathbf{f}(\cdot)$ and $\mathbf{g}(\cdot)$ are the (nonlinear) state transition and measurement functions derived in the following section.

State Transition Function: The state transition function predicts how the internal states of the battery change, given the current input at each time step. In the considered second-order ECM, the states consist of the following:

$$\mathbf{x}_k = \begin{bmatrix} \mathrm{SOC}_k & U_{\mathrm{RC1},k} & U_{\mathrm{RC2},k} \end{bmatrix}^{\mathsf{T}}$$

- SOC_k: the state of charge at time step k.
- $U_{\mathrm{RC1},k}$: the voltage across the first RC branch at time step k.
- $U_{\mathrm{RC2},k}$: the voltage across the second RC branch at time step k.

State of Charge (SOC): The SOC represents the ratio of remaining charge to the maximum usable charge and is typically expressed as a percentage. The SOC is updated based on the net charge flowing into or out of the battery. Under the assumption of constant current i_k over the sample period Δt, and neglecting efficiency and self-discharge, the SOC is updated via Coulomb counting and forward-Euler discretizations as follows:

$$\mathrm{SOC}_{k+1} = \mathrm{SOC}_k - \frac{\Delta t}{C_\mathrm{p}} \frac{i_k}{3600} \tag{2}$$

where

- i_k is the terminal current (positive for discharge).
- C_p is the present capacity of the battery in ampere-hours (Ah).

- The factor 3600 converts seconds to hours.

RC Branch Voltages: The two RC branches in the ECM capture the transient behavior of the cell voltage during load changes. The dynamics of each RC branch are modeled using a first-order linear differential equation derived from Kirchhoff's laws

$$\frac{dU_{\mathrm{RC}i}(t)}{dt} = -\frac{1}{R_i C_i} U_{\mathrm{RC}i}(t) + \frac{1}{C_i} i(t), \quad i \in \{1,2\}$$

This equation models the voltage across a capacitor C_i in parallel with a resistor R_i under current excitation. Discretizing using the exact exponential solution results in the following:

$$U_{\mathrm{RC}i,k+1} = e^{-\Delta t/(R_i C_i)} U_{\mathrm{RC}i,k} + \left(1 - e^{-\Delta t/(R_i C_i)}\right) R_i i_k \tag{3}$$

This equation reveals that each RC voltage decays exponentially with a time constant $\tau_i = R_i C_i$, and the steady-state value is driven by $R_i i_k$.

State Transition Vector Function: By combining Equations (2) and (3) for both RC branches, the full nonlinear transition function is written compactly as follows:

$$f(\mathbf{x}_k, u_k) = \begin{bmatrix} x_k(1) - \dfrac{\Delta t}{3600 \cdot \mathrm{C_p}} \cdot u_k \\ x_k(2) \cdot e^{-\Delta t/(R_1 C_1)} + \left(1 - e^{-\Delta t/(R_1 C_1)}\right) R_1 u_k \\ x_k(3) \cdot e^{-\Delta t/(R_2 C_2)} + \left(1 - e^{-\Delta t/(R_2 C_2)}\right) R_2 u_k \end{bmatrix} \tag{4}$$

Measurement Function: The terminal voltage U_k is the observable output of the battery system and is computed by applying Kirchhoff's voltage law (KVL) along the circuit:

$$y_k = U_{\mathrm{OCV}}(\mathrm{SOC}_k) - U_{\mathrm{RC1},k} - U_{\mathrm{RC2},k} - R_0 i_k \tag{5}$$

- $U_{\mathrm{OCV}}(\mathrm{SOC}_k)$: the open-circuit voltage as a nonlinear function of the SOC.
- $U_{\mathrm{RC1},k}$ and $U_{\mathrm{RC2},k}$: transient voltage drops from the RC branches.
- $R_0 i_k$: instantaneous ohmic drop.

The nonlinearity in the measurement function arises solely from the $U_{\mathrm{OCV}}(\mathrm{SOC})$ term. All other terms are linear with respect to the states and input. The OCV–SOC curve is typically obtained offline and approximated using high-order polynomials or spline fits.

State of Health (SOH): Battery aging leads to a gradual reduction in usable capacity, denoted by C_p, relative to the rated or nominal capacity C_0. The SOH is therefore defined as the ratio of these two quantities:

$$\mathrm{SOH} = 100 \cdot \frac{\mathrm{C_p}}{\mathrm{C_0}} \quad [\%] \tag{6}$$

where

- C_p is the estimated present capacity (Ah).
- C_0 is the manufacturer-specified fresh-cell rated capacity (Ah).

Fast-varying quantities such as the SOC and the RC voltages are treated as *states*, whereas slowly varying quantities such as C_p and R_0 are considered *parameters* to be adapted over the cell's lifetime.

2.4. Estimation Methods

Estimation methods are mathematical tools that are used to predict the internal states or parameters of a system based on noisy measurements of a few selected states under un-

certain model dynamics. One of the most foundational estimation algorithms is the Kalman filter, which was originally introduced by Rudolf E. Kalman [44]. It offers a recursive method for estimating the states of linear dynamic systems affected by Gaussian noise. Due to its computational efficiency and optimal performance under linear Gaussian conditions, this filter has found widespread application in numerous engineering disciplines.

Discrete-time Kalman filter recursion utilizes the following system model:

$$\mathbf{x}_k = \mathbf{A}_{k-1}\,\mathbf{x}_{k-1} + \mathbf{B}_{k-1}\,\mathbf{u}_{k-1} + \mathbf{w}_{k-1} \tag{7}$$

$$\mathbf{y}_k = \mathbf{C}_k\,\mathbf{x}_k + \mathbf{v}_k \tag{8}$$

where $\mathbf{w}_{k-1} \sim \mathcal{N}(\mathbf{0},\, \mathbf{Q}_{k-1})$ and $\mathbf{v}_k \sim \mathcal{N}(\mathbf{0},\, \mathbf{R}_k)$ are mutually uncorrelated white Gaussian noises. Afterwards, the Kalman filter proceeds with the time update (prediction) and measurement update (correction) steps. These steps propagate the state estimate $\hat{\mathbf{x}}$ and its error covariance $\mathbf{P}$

$$\text{Time update (prediction):} \quad \hat{\mathbf{x}}_{k|k-1} = \mathbf{A}_{k-1}\,\hat{\mathbf{x}}_{k-1|k-1} + \mathbf{B}_{k-1}\,\mathbf{u}_{k-1} \tag{9}$$

$$\mathbf{P}_{k|k-1} = \mathbf{A}_{k-1}\,\mathbf{P}_{k-1|k-1}\,\mathbf{A}_{k-1}^{\mathsf{T}} + \mathbf{Q}_{k-1} \tag{10}$$

$$\text{Measurement update (correction):} \quad e_k = \mathbf{y}_k - \mathbf{g}\big(\hat{\mathbf{x}}_{k|k-1}, \mathbf{u}_k\big) \tag{11}$$

$$\mathbf{K}_k = \mathbf{P}_{k|k-1}\,\mathbf{C}_k^{\mathsf{T}}\left(\mathbf{C}_k\,\mathbf{P}_{k|k-1}\,\mathbf{C}_k^{\mathsf{T}} + \mathbf{R}_k\right)^{-1} \tag{12}$$

$$\hat{\mathbf{x}}_{k|k} = \hat{\mathbf{x}}_{k|k-1} + \mathbf{K}_k e_k \tag{13}$$

$$\mathbf{P}_{k|k} = \left(\mathbf{I} - \mathbf{K}_k\,\mathbf{C}_k\right)\mathbf{P}_{k|k-1} \tag{14}$$

To address nonlinear systems, numerous extensions to the original Kalman filter have been developed. In this paper, four variants of these nonlinear extensions are studied. Sections 2.4.1 and 2.4.2 review the *single-observer* forms that operate on the nonlinear ECM of Equation (1). Sections 2.4.3 and 2.4.4 then extend these baselines to the *dual* architecture that jointly tracks fast states and slow aging parameters.

2.4.1. Extended Kalman Filter (EKF)

The extended Kalman filter adapts the original linear Gaussian framework to the nonlinear state–space model. Because the mappings $\mathbf{f}(\cdot)$ and $\mathbf{h}(\cdot)$ are nonlinear, the joint distribution of the state and measurement is no longer Gaussian after propagation. The EKF locally approximates the mappings with their first-order Taylor expansions about the most recent state estimate. The Jacobian matrices of the discrete transition and measurement functions are derived as follows:

$$\mathbf{A}_{k-1} = \left.\frac{\partial \mathbf{f}}{\partial \mathbf{x}}\right|_{\hat{\mathbf{x}}_{k-1|k-1},\,\mathbf{u}_{k-1}} = \begin{bmatrix} 1 & 0 & 0 \\ 0 & e^{-\frac{dt}{R_1 C_1}} & 0 \\ 0 & 0 & e^{-\frac{dt}{R_2 C_2}} \end{bmatrix} \tag{15}$$

$$\mathbf{C}_k = \left.\frac{\partial \mathbf{g}}{\partial \mathbf{x}}\right|_{\hat{\mathbf{x}}_{k|k-1}} = \begin{bmatrix} \left.\frac{\partial U_{OCV}}{\partial SOC}\right|_{\hat{x}_{k|k-1}} & 1 & 1 \end{bmatrix} \tag{16}$$

It is worth noting that the performance of the EKF relies on the assumption that system nonlinearities remain moderate, as significant deviations from linearity introduce larger approximation errors into the estimation process.

Afterwards, the predicted mean is obtained by evaluating the nonlinear model in the previous estimated state and the current input.

$$\hat{\mathbf{x}}_{k|k-1} = \mathbf{f}\big(\hat{\mathbf{x}}_{k-1|k-1}, \mathbf{u}_{k-1}\big) \tag{17}$$

The covariance matrix is mapped through the linearized system dynamics (14).

After a new observation $\mathbf{y}_k$ arrives, the innovation, Kalman gain, and posterior statistics are calculated based on the measurement update step of the standard Kalman filter (11)–(14).

In cases where both the process dynamics and measurement equations are linear, this procedure reduces directly to the standard discrete-time Kalman filter.

2.4.2. Unscented Kalman Filter (UKF)

The unscented Kalman filter utilizes the *unscented transform*, which represents a Gaussian random vector by a deterministic set of *sigma-points*. Each sigma-point is propagated through the nonlinear process and measurement models, and the posterior statistics are reconstructed from the transformed points. This method removes the need for the Jacobian calculation required by the EKF while capturing the mean and covariance of any smooth nonlinear mapping with second-order accuracy.

For an n-dimensional state, the UKF employs $2n+1$ sigma-points $\chi_{k-1}^{(i)}$. These points are chosen to capture the mean and covariance of the state distribution. Each sigma-point has an associated weight for computing the mean ($w_i^{(m)}$) and for computing the covariance ($w_i^{(c)}$). These weights are determined by three scaling parameters α, β, and κ, as follows:

$$\begin{aligned} \lambda &= \alpha^2(n+\kappa) - n, & w_0^{(m)} &= \frac{\lambda}{n+\lambda}, \\ w_0^{(c)} &= w_0^{(m)} + (1-\alpha^2+\beta), & w_i^{(m)} &= w_i^{(c)} = \frac{1}{2(n+\lambda)} \ (i \geq 1). \end{aligned} \tag{18}$$

The sigma-points at time $k-1$ are derived as follows:

$$\begin{aligned} \chi_{k-1}^{(0)} &= \hat{\mathbf{x}}_{k-1|k-1} \\ \chi_{k-1}^{(i)} &= \hat{\mathbf{x}}_{k-1|k-1} + \sqrt{n+\lambda}\,\left[\sqrt{\mathbf{P}}\right]_i, \qquad i = 1,\ldots,n, \\ \chi_{k-1}^{(i+n)} &= \hat{\mathbf{x}}_{k-1|k-1} - \sqrt{n+\lambda}\,\left[\sqrt{\mathbf{P}}\right]_i, \qquad i = 1,\ldots,n. \end{aligned} \tag{19}$$

where $\sqrt{\mathbf{P}}$ is the matrix square root of the covariance.

Each sigma-point is then propagated through the nonlinear process model $\mathbf{f}(\cdot, \mathbf{u}_{k-1})$

$$\chi_{k|k-1}^{(i)} = \mathbf{f}\big(\chi_{k-1}^{(i)}, \mathbf{u}_{k-1}\big),$$

and the predicted mean and covariance are derived as follows:

$$\hat{\mathbf{x}}_{k|k-1} = \sum_{i=0}^{2n} w_i^{(m)}\, \chi_{k|k-1}^{(i)} \qquad \mathbf{P}_{k|k-1} = \sum_{i=0}^{2n} w_i^{(c)} \big(\chi_{k|k-1}^{(i)} - \hat{\mathbf{x}}_{k|k-1}\big)(\cdot)^{\mathsf{T}} + \mathbf{Q}_{k-1}. \tag{20}$$

By applying the measurement model $\mathbf{g}(\cdot)$, each predicted sigma-point is propagated through the measurement function

$$\gamma_k^{(i)} = \mathbf{g}\big(\chi_{k|k-1}^{(i)}\big) \tag{21}$$

This allows for deriving the predicted measurement mean $\hat{\mathbf{y}}_{k|k-1}$, the cross-covariance $\mathbf{P_{xy}}$, and the innovation covariance $\mathbf{S}_k$ values:

$$\begin{aligned}\hat{\mathbf{y}}_{k|k-1} &= \sum_{i=0}^{2n} w_i^{(m)}\, \gamma_{k|k-1}^{(i)},\\ \mathbf{P}_{xy} &= \sum_{i=0}^{2n} w_i^{(c)} \left(\chi_{k|k-1}^{(i)} - \hat{\mathbf{x}}_{k|k-1}\right)\left(\gamma_{k|k-1}^{(i)} - \hat{\mathbf{y}}_{k|k-1}\right)^{\mathsf{T}},\\ \mathbf{S}_k &= \sum_{i=0}^{2n} w_i^{(c)} \left(\gamma_{k|k-1}^{(i)} - \hat{\mathbf{y}}_{k|k-1}\right)(\cdot)^{\mathsf{T}}.\end{aligned} \tag{22}$$

From these, the Kalman gain and corrected state and covariance estimations are derived as follows:

$$\begin{aligned}\mathbf{K}_k &= \mathbf{P_{xy}}\, \mathbf{S}_k^{-1},\\ \hat{\mathbf{x}}_{k|k} &= \hat{\mathbf{x}}_{k|k-1} + \mathbf{K}_k\left(\mathbf{y}_k - \hat{\mathbf{y}}_{k|k-1}\right),\\ \mathbf{P}_{k|k} &= \mathbf{P}_{k|k-1} - \mathbf{K}_k \mathbf{S}_k \mathbf{K}_k^{\mathsf{T}}\end{aligned} \tag{23}$$

2.4.3. Dual Extended Kalman Filter (DEKF)

To account for battery aging, the DEKF addresses the estimation problem by dividing it into two parallel estimation tasks. The state estimation component follows the previously outlined EKF steps to estimate essential internal states, such as the SOC and RC voltage dynamics. Concurrently, the parameter estimation module operates in parallel, dedicated to identifying battery parameters, such as the series resistance R_0 and the present battery capacity C_p. These parameters are typically modeled as constant or slowly evolving states, with small process noise enabling gradual adaptation.

Consequently, the DEKF comprises two coupled EKFs running simultaneously: one estimates the dynamic state while assuming known parameters, and the other refines the parameter estimates using the latest state predictions as input.

For the ECM with the following state and parameter vectors,

$$\mathbf{x}_k = \begin{bmatrix} SOC_k & U_{\mathrm{RC1},k} & U_{\mathrm{RC2},k}\end{bmatrix}^{\mathsf{T}} \qquad \boldsymbol{\theta}_k = \begin{bmatrix} R_{0,k} & C_{P,k}\end{bmatrix}^{\mathsf{T}} \tag{24}$$

The dual architecture prescribes two coupled nonlinear process models where the state estimation utilizes the state transition model derived from the ECM, and the parameter estimation treats the dynamics of the slowly evolving parameters as a random walk:

$$\boldsymbol{\theta}_k = \boldsymbol{\theta}_{k-1} + \mathbf{w}_{k-1}^{\theta} \qquad \mathbf{w}_{k-1}^{\theta} \sim \mathcal{N}\left(\mathbf{0}, \mathbf{Q}_{k-1}^{\theta}\right), \tag{25}$$

where $\mathbf{Q}_{k-1}^{\theta}$ is diagonal and orders of magnitude smaller than $\mathbf{Q}_{k-1}^{x}$, reflecting the slow drift of R_0 and C_P.

Both filters observe the same terminal voltage measurement in their correction step:

$$\mathbf{y}_k = \mathbf{g}\left(\mathbf{x}_k, \mathbf{u}_k, \boldsymbol{\theta}_k\right) + \mathbf{v}_k \qquad \mathbf{v}_k \sim \mathcal{N}\left(\mathbf{0}, \mathbf{R}_k^{\theta}\right). \tag{26}$$

At each sample time k, the DEKF executes the following five steps. The notation $(\cdot)^x$ and $(\cdot)^\theta$ distinguishes state and parameter filter quantities.

1. **State filter prediction:** $\hat{\mathbf{x}}_{k-1|k-1}$ is propagated through $\mathbf{f}(\cdot)$ using the most recent parameter estimate $\hat{\boldsymbol{\theta}}_{k-1|k-1}$. A first-order linearization about this operating point produces the Jacobian that updates the state covariance $\mathbf{P}^x$

$$\mathbf{A}_{k-1}^{x} = \left.\frac{\partial \mathbf{f}}{\partial \mathbf{x}}\right|_{\left(\hat{\mathbf{x}}_{k-1|k-1}, \hat{\boldsymbol{\theta}}_{k-1|k-1}, \mathbf{u}_{k-1}\right)} \tag{27}$$

2. **State filter correction:** The innovation is computed, and $\hat{\mathbf{x}}_{k|k}$, $\mathbf{P}_{k|k}^{x}$ is updated with the linearized measurement matrix

$$\boldsymbol{e}_k^x = \mathbf{y}_k - \mathbf{g}\left(\hat{\mathbf{x}}_{k|k-1}, \hat{\boldsymbol{\theta}}_{k-1|k-1}\right) \tag{28}$$

$$\mathbf{C}_k^x = \left.\frac{\partial \mathbf{g}}{\partial \mathbf{x}}\right|_{\left(\hat{\mathbf{x}}_{k|k-1}, \hat{\boldsymbol{\theta}}_{k-1|k-1}\right)} \tag{29}$$

3. **Parameter filter prediction:** $\hat{\boldsymbol{\theta}}_{k-1|k-1}$ is carried forward as $\hat{\boldsymbol{\theta}}_{k|k-1}$, and its covariance is increased by $\mathbf{Q}_{k-1}^{\theta}$, accounting for potential drift.

$$\hat{\boldsymbol{\theta}}_{k|k-1} = \hat{\boldsymbol{\theta}}_{k-1|k-1} \qquad \mathbf{P}_{k|k-1}^{\boldsymbol{\theta}} = \mathbf{P}_{k-1|k-1}^{\boldsymbol{\theta}} + \mathbf{Q}_{k-1}^{\theta} \tag{30}$$

4. **Parameter filter correction:** Linearizing the measurement function with respect to $\boldsymbol{\theta}$ at the current operating point estimated at step (2) gives the measurement model required by the EKF:

$$\mathbf{e}_k^{\theta} = \mathbf{y}_k - \mathbf{g}\left(\hat{\mathbf{x}}_{k|k}, \hat{\boldsymbol{\theta}}_{k|k-1}\right) \tag{31}$$

$$\mathbf{C}_k^{\theta} = \left.\frac{\partial \mathbf{g}}{\partial \boldsymbol{\theta}}\right|_{\left(\hat{\mathbf{x}}_{k|k}, \hat{\boldsymbol{\theta}}_{k|k-1}\right)} \tag{32}$$

Applying the standard EKF measurement update yields

$$\mathbf{K}_k^{\theta} = \mathbf{P}_{k|k-1}^{\boldsymbol{\theta}} \mathbf{C}_k^{\theta\top} \left(\mathbf{C}_k^{\theta} \mathbf{P}_{k|k-1}^{\boldsymbol{\theta}} \mathbf{C}_k^{\theta\top} + \mathbf{R}_k^{\theta}\right)^{-1} \tag{33}$$

$$\hat{\boldsymbol{\theta}}_{k|k} = \hat{\boldsymbol{\theta}}_{k|k-1} + \mathbf{K}_k^{\theta}\, \mathbf{e}_k^{\theta} \tag{34}$$

$$\mathbf{P}_{k|k}^{\boldsymbol{\theta}} = \left(\mathbf{I} - \mathbf{K}_k^{\theta} \mathbf{C}_k^{\theta}\right) \mathbf{P}_{k|k-1}^{\boldsymbol{\theta}} \tag{35}$$

These equations close the parameter loop by fusing the innovation-derived measurement with the prior $\hat{\boldsymbol{\theta}}_{k|k-1}$, producing the updated estimate $\hat{\boldsymbol{\theta}}_{k|k}$ and its covariance $\mathbf{P}_{k|k}^{\theta}$.

Jacobian Derivation for the Linearized ECM

The dual-observer architecture employs four Jacobians:

- $\mathbf{A}_{k-1}^{x}$: State transition Jacobian for the **state** filter.
- $\mathbf{C}_k^{x}$: Measurement Jacobian with respect to the states.
- $\mathbf{A}_{k-1}^{\theta}$: Parameter transition Jacobian for the **parameter** filter.
- $\hat{\mathbf{C}}_k^{\theta}$: Measurement Jacobian with respect to the aging parameters.

$\mathbf{A}_{k-1}^{x}$ and $\mathbf{C}_k^{x}$ are unchanged because the state observer in the dual filter mirrors the single-observer EKF in Section 2.4.1; therefore, its linearization matrices are identical, which are the expressions already given in Equations (15) and (16). The dual filter just refreshes the numerical values with the *current* parameter estimates at each step.

The parameter transition Jacobian $\mathbf{A}_{k-1}^{\theta}$ is calculated as an identity matrix, because the aging parameters follow a random walk model, which is linear with unit gain, with

$n_\theta = 2$ for the pair $\{R_0, C_P\}$. This means that in the prediction step, the mean of $\boldsymbol{\theta}$ is simply copied forward while its covariance is increased by $\mathbf{Q}^{\theta}_{k-1}$.

$\hat{\mathbf{C}}^{\theta}_{k}$, which is the the parameter-to-measurement Jacobian, must capture both the direct effect of R_0 on the ohmic drop and the indirect influence of R_0 and C_P through the state trajectory. It is defined by the total derivative:

$$\hat{\mathbf{C}}^{\theta}_{k} = \left.\frac{d\,\mathbf{g}\big(\hat{\mathbf{x}}_{k|k-1}, \mathbf{u}_k, \boldsymbol{\theta}\big)}{d\boldsymbol{\theta}}\right|_{\boldsymbol{\theta}=\hat{\boldsymbol{\theta}}_{k|k-1}} \tag{36a}$$

$$\frac{d\,\mathbf{g}\big(\hat{\mathbf{x}}_{k|k-1}, \mathbf{u}_k, \boldsymbol{\theta}\big)}{d\boldsymbol{\theta}} = \frac{\partial \mathbf{g}\big(\hat{\mathbf{x}}_{k|k-1}, \mathbf{u}_k, \boldsymbol{\theta}\big)}{\partial \boldsymbol{\theta}} + \frac{\partial \mathbf{g}\big(\hat{\mathbf{x}}_{k|k-1}, \mathbf{u}_k, \boldsymbol{\theta}\big)}{\partial \hat{\mathbf{x}}_{\mathbf{k}|\mathbf{k-1}}} \frac{d\hat{\mathbf{x}}_{k|k-1}}{d\boldsymbol{\theta}} \tag{36b}$$

With the state sensitivity matrix $d\hat{\mathbf{x}}/d\boldsymbol{\theta}$ propagated by

$$\frac{d\hat{\mathbf{x}}_{k|k-1}}{d\boldsymbol{\theta}} = \frac{\partial \mathbf{f}\big(\hat{\mathbf{x}}_{k-1|k-1}, \mathbf{u}_{k-1}, \boldsymbol{\theta}\big)}{\partial \boldsymbol{\theta}} + \frac{\partial \mathbf{f}\big(\hat{\mathbf{x}}_{k-1|k-1}, \mathbf{u}_{k-1}, \boldsymbol{\theta}\big)}{\partial \hat{\mathbf{x}}_{\mathbf{k}|\mathbf{k-1}}} \frac{d\hat{\mathbf{x}}_{k-1|k-1}}{d\boldsymbol{\theta}} \tag{37a}$$

$$\frac{d\hat{\mathbf{x}}_{k-1|k-1}}{d\boldsymbol{\theta}} = \frac{d\hat{\mathbf{x}}_{k-1|k-2}}{d\boldsymbol{\theta}} - \mathbf{K}^{x}_{k-1} \frac{d\,\mathbf{g}\big(\hat{\mathbf{x}}_{k-1|k-2}, \mathbf{u}_{k-1}, \boldsymbol{\theta}\big)}{d\boldsymbol{\theta}} \tag{37b}$$

This can be calculated for each time stamp by starting from $\frac{d\hat{\mathbf{x}}_0}{d\boldsymbol{\theta}} = \mathbf{0}$ and $\frac{d\,\mathbf{g}(\hat{\mathbf{x}}_0, \mathbf{u}_0, \boldsymbol{\theta})}{d\boldsymbol{\theta}} = \mathbf{0}$. The remaining required partial derivatives are represented as follows:

$$\frac{\partial \mathbf{g}\big(\hat{\mathbf{x}}_{k|k-1}, \mathbf{u}_k, \boldsymbol{\theta}\big)}{\partial \boldsymbol{\theta}} = \begin{bmatrix} 0 & i_k \end{bmatrix} \qquad \frac{\partial \mathbf{g}\big(\hat{\mathbf{x}}_{k|k-1}, \mathbf{u}_k, \boldsymbol{\theta}\big)}{\partial \hat{\mathbf{x}}_{\mathbf{k}|\mathbf{k-1}}} = \begin{bmatrix} \frac{\partial U_{\mathrm{OCV}}}{\partial \mathrm{SOC}}\big|_{\hat{\mathbf{x}}_{k|k-1}} & 1 & 1 \end{bmatrix}$$

$$\frac{\partial \mathbf{f}\big(\hat{\mathbf{x}}_{k-1|k-1}, \mathbf{u}_{k-1}, \boldsymbol{\theta}\big)}{\partial \boldsymbol{\theta}} = \begin{bmatrix} -\frac{\Delta t}{C_P^2}\, i_{k-1} & 0 \\ 0 & 0 \\ 0 & 0 \end{bmatrix}$$

$$\frac{\partial \mathbf{f}\big(\hat{\mathbf{x}}_{k-1|k-1}, \mathbf{u}_{k-1}, \boldsymbol{\theta}\big)}{\partial \hat{\mathbf{x}}_{\mathbf{k}|\mathbf{k-1}}} = \mathrm{diag}\big(1,\, e^{-\Delta t/(R_1 C_1)},\, e^{-\Delta t/(R_2 C_2)}\big)$$

Both EKFs start from a common time origin with $\hat{\mathbf{x}}_{0|0} = \mathbf{x}_0, \hat{\boldsymbol{\theta}}_{0|0} = \boldsymbol{\theta}_0$, which are the initial estimates. The covariance blocks $\mathbf{P}^{x}_{0|0}$ and $\mathbf{P}^{\theta}_{0|0}$ are set independently; no cross-terms are maintained since the filters exchange only their posterior means. The resulting dual-loop structure allows for the rapid correction of high-frequency state dynamics while slowly adapting to long-term parameter drift.

2.4.4. Dual Unscented Kalman Filter (DUKF)

The DUKF follows the dual-observer layout of the DEKF but substitutes every first-order Jacobian linearization with an unscented transform. Both observers require only matrix–vector products and Cholesky factorizations of the predicted covariances, which removes the need for calculating Jacobians. Because the parameter dimension n_θ is small, the added complexity of using an independent sigma set is acceptable.

Both the state and parameter observers reuse the sigma-point construction and weighting rules of Equations (18) and (19). The number of sigma points for the state variables $n_x = 3$ and the aging parameters $n_\theta = 2$ are denoted by $L_x = 2n_x + 1$ and $L_\theta = 2n_\theta + 1$, respectively. At each sampling instant, the DUKF executes the four stages outlined below.

1. **State prediction.** L_x sigma-points are generated around $\left(\hat{\mathbf{x}}_{k-1|k-1}, \mathbf{P}^{x}_{k-1|k-1}\right)$, and each is propagated through the nonlinear transition model while keeping the latest parameter estimate $\hat{\boldsymbol{\theta}}_{k-1|k-1}$:

$$\mathcal{X}^{x(i)}_{k|k-1} = \mathbf{f}\left(\mathcal{X}^{x(i)}_{k-1}, \mathbf{u}_{k-1}, \hat{\boldsymbol{\theta}}_{k-1|k-1}\right).$$

   The predicted mean and covariance are derived using Equation (20) with $\mathbf{Q}_{k-1} \rightarrow \mathbf{Q}^{x}_{k-1}$.

2. **State correction.** The predicted sigma-points are transformed through the measurement function $\gamma^{x(i)}_{k} = \mathbf{g}\left(\mathcal{X}^{x(i)}_{k|k-1}, \hat{\boldsymbol{\theta}}_{k-1|k-1}\right)$, and the UKF update of Equation (23) is applied. The resulting innovation $\boldsymbol{e}^{x}_{k} = \mathbf{y}_k - \hat{\mathbf{y}}_{k|k-1}$ is also used in the fourth stage.

3. **Parameter prediction.** Since the aging parameters follow the random walk model, each parameter sigma-point undergoes identity propagation: $\mathcal{X}^{\theta(i)}_{k|k-1} = \mathcal{X}^{\theta(i)}_{k-1}$. The predicted mean and covariance are given by Equation (20) with $\mathbf{Q}_{k-1} \rightarrow \mathbf{Q}^{\theta}_{k-1}$.

4. **Parameter correction.** The state innovation e^{x}_{k} in step two is utilized as a measurement of $\boldsymbol{\theta}$. Each parameter sigma-point is evaluated in the voltage model at the latest corrected state:

$$\gamma^{\theta(i)}_{k} = \mathbf{g}\left(\hat{\mathbf{x}}_{k|k}, \mathcal{X}^{\theta(i)}_{k|k-1}\right).$$

   Afterwards, Equations (22) and (23) are utilized with $\mathbf{R}_k \rightarrow \mathbf{R}^{\theta}_{k}$ to obtain $\hat{\boldsymbol{\theta}}_{k|k}$, $\mathbf{P}^{\theta}_{k|k}$.

2.5. Simulation Environment

All filters were implemented in MATLAB R2024b/Simulink 23.2 and executed with a fixed-step discrete solver ($\Delta t = 0.1$ s) on an Intel Core i7-12700H CPU (single thread). Wall-clock runtimes were measured with `tic/toc` over the entire drive cycle.

3. Results and Discussion

3.1. Tuning the Filter Parameters

3.1.1. Importance of Covariance Optimization

The performance of Kalman-filter-based estimators critically depends on the proper tuning of the process noise covariance (Q) and measurement noise covariance (R), where Q captures the uncertainty due to imperfections in the system model, and R represents the trustworthiness and precision of the sensor data. Poor tuning often produces drift, bias, or divergence in SOC and SOH estimates for battery systems [3]. Although these matrices represent physical attributes of the system dynamics and measurement devices, accurately determining their values from theoretical models and instrument specifications is challenging due to numerous influencing factors and system complexities. Therefore, relying only on trial-and-error approaches lacks consistency and scalability. As a result, automated methods for covariance optimization are essential to ensure robust performance across various operational conditions.

In addition to influencing filter stability, the process and measurement covariance matrices determine how uncertainty is represented and propagated within Kalman-filter-based estimators. The evolving state and parameter covariance matrices quantify the confidence bounds of the SOC and C_p estimates, providing a probabilistic measure of their reliability. Under model mismatch conditions, such as a discrepancy between the assumed battery model and the actual cell behavior, the process noise covariance Q serves as a compensatory term that inflates the estimated uncertainty, thereby preventing the filter from becoming overconfident in biased predictions. Similarly, the measurement noise covariance R adjusts the reliance on sensor data relative to model predictions, ensuring an appropriate

balance between the two sources of information. An increase in the posterior covariance of either the state or parameter estimates reflects reduced estimator confidence due to unmodeled dynamics or measurement inconsistencies. Through covariance optimization, the estimators adapt this uncertainty representation to maintain robustness and consistent estimation accuracy under varying operating and modeling conditions.

3.1.2. Optimization Problem Formulation

The covariance selection task was formulated as a constrained nonlinear minimization problem.

$$\min_{\mathbf{x}\in\mathbb{R}^n} J(\mathbf{x}), \qquad \mathbf{x} = \log_{10}\big(\mathrm{vec}\{Q^x, R^x, Q^\theta, R^\theta\}\big). \tag{38}$$

The cost function was designed in order to prioritize SOC accuracy before parameter accuracy, preventing solutions that trade SOC errors for a large capacity gain.

$$J \;=\; \frac{1}{N}\sum_{k=1}^{N}\Big(\mathrm{RMSE}\big(\widehat{C_{\mathrm{p}}}_k - C_p\big) \;+\; 2\;\mathrm{RMSE}\big(\widehat{\mathrm{SOC}}_k - \mathrm{SOC}_k\big)\Big). \tag{39}$$

where $\widehat{C_{\mathrm{p}}}$ and $\widehat{\mathrm{SOC}}$ are the estimated total capacity and state of charge, respectively. Only the diagonal elements of the covariance matrices were treated as tuning parameters, and the off-diagonal elements were fixed to zero to reduce the parameter space.

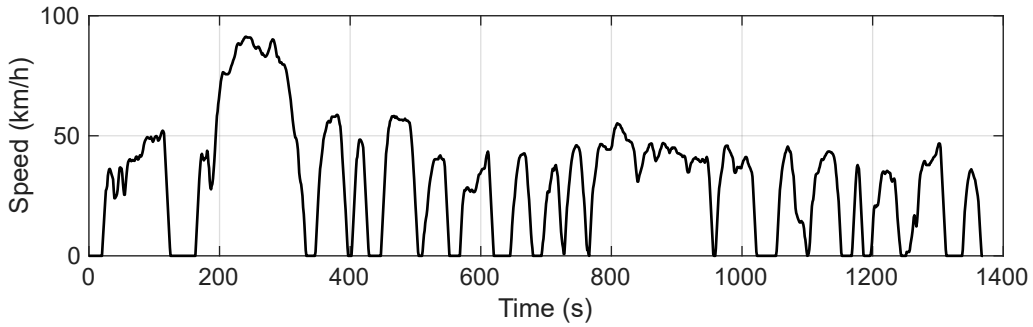
The formulation of the optimization problem is influenced by the relatively large search space for Q and R, which can span 12–14 orders of magnitude, from slow temperature drift states to fast electrical states. Therefore, direct optimization in linear space results in an ill-conditioned optimization space where a one-unit step in a large variance value can overweight the changes in a smaller value and corrupt the gradient search. Taking the base-10 logarithm converts multiplicative changes into additive ones, giving every order of magnitude equal numerical weight. Log-space also smooths the objective surface by reducing local traps and improving the conditioning of the finite-difference Jacobian used by the interior-point solver.

3.1.3. Dataset and Disturbances

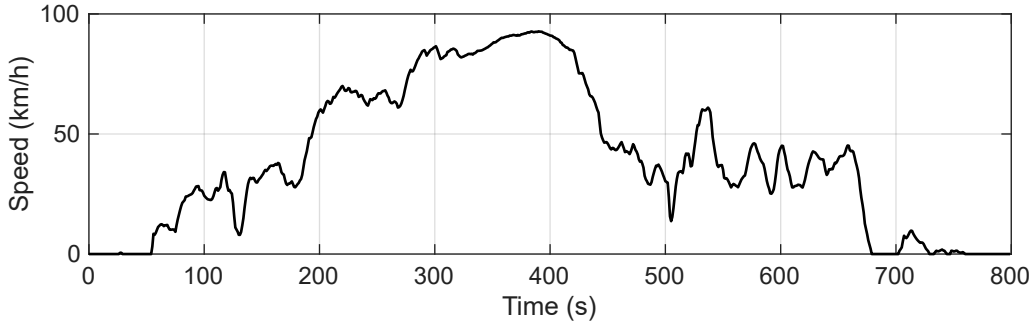
The training process was designed to capture a wide range of driving conditions and initialization errors, ensuring the robust generalization of the estimator in real-world scenarios. Two distinct drive cycles were utilized to reflect operational variability. The first, the Urban Dynamometer Driving Schedule (UDDS, Figure 2a), models stop-and-go urban traffic typical of light-duty vehicles and is characterized by frequent accelerations and decelerations. The CLUST7 cycle (Figure 2b) was constructed from the ecoDrive database [45], which recorded over 200,000 journeys from 1085 vehicles registered in France, Spain, Germany, the United Kingdom, and Italy from the start of 2015 to the end of March 2016. The cycle was obtained using a clustering algorithm [46] and is representative of mixed urban/rural driving conditions.

To further improve the robustness of the estimator, initialization errors were introduced in both the SOC and battery capacity estimates. The training dataset included scenarios with initial SOC deviations of −40%, 0%, and 20% and initial capacity deviations of −40%, 0%, and 40%, reflecting the real-world challenge where the true initial state is not precisely known in online estimation tasks.

By performing optimization under dynamic variability and state uncertainty, the training rewarded the extraction of covariance matrices that enabled consistent estimator performance. This resulted in faster and more reliable convergence across a broader range of initial conditions, minimizing bias accumulation and enhancing real-world applicability.



(**a**)



(**b**)

Figure 2. The drive cycles that were employed: (**a**) The UDDS driving cycle. (**b**) The CLUST7 real driving cycle.

3.1.4. Optimization Methodology

MATLAB's `fmincon` (interior-point) solver was used, with gradients approximated by central finite differences (`StepTolerance` = 10^{-12}). Parallel evaluation via `parfor` reduced wall-time sixfold on a six-core workstation. The dual filters were tuned with a two-stage procedure, as detailed in Table 1.

Table 1. Two-stage covariance optimization strategy.

Stage	Filters	Decision Vector	Description
1	EKF/UKF	$(Q^x_{1:3},\ R^x)$	Optimize the fast SOC estimator independently.
2	DEKF/DUKF	$(Q^x_{1:3},\ R^x,\ Q^\theta_{1:2},\ R^\theta)$	Jointly optimize dual estimators, accounting for SOC–SOH interaction.

Convergence was typically reached within 800 cost function evaluations. Representative optimal covariance values, obtained using both UDDS and CLUST7 driving cycles under varying initial estimation errors, are reported in Table 2.

Table 2. Optimized covariances.

Filter	Quantity	Symbol	Unit	Value
EKF	SOC variance	Q^x_1	-	6.8×10^{-14}
	RC1 voltage variance	Q^x_2	V^2	3.6×10^{-6}
	RC2 voltage variance	Q^x_3	V^2	1.0×10^{-6}
	Voltage variance (state filter)	R^x	V^2	1.1×10^{-3}

Table 2. *Cont.*

Filter	Quantity	Symbol	Unit	Value
UKF	SOC variance	Q_1^x	-	8.6×10^{-14}
	RC1 voltage variance	Q_2^x	V^2	2.0×10^{-6}
	RC2 voltage variance	Q_3^x	V^2	3.0×10^{-7}
	Voltage variance (state filter)	R^x	V^2	4.7×10^{-4}
DEKF	SOC variance	Q_1^x	-	1.0×10^{-8}
	RC1 voltage variance	Q_2^x	V^2	6.1×10^{-6}
	RC2 voltage variance	Q_3^x	V^2	6.1×10^{-6}
	Measurement variance	R^x	V^2	2.3×10^{-4}
	Resistance variance	Q_1^θ	Ω^2	3.9×10^{-6}
	Capacity variance	Q_2^θ	$(Ah)^2$	7.5×10^{-11}
	Voltage variance (param. filter)	R^θ	V^2	1.7×10^{-5}
DUKF	SOC variance	Q_1^x	-	1.0×10^{-8}
	RC1 voltage variance	Q_2^x	V^2	3.3×10^{-6}
	RC2 voltage variance	Q_3^x	V^2	3.3×10^{-6}
	Measurement variance	R^x	V^2	2.0×10^{-3}
	Resistance variance	Q_1^θ	Ω^2	1.0×10^{-3}
	Capacity variance	Q_2^θ	$(Ah)^2$	7.6×10^{-8}
	Voltage variance (param. filter)	R^θ	V^2	1.0×10^{-1}

The parameters are archived in a `.mat` file for subsequent software-in-the-loop validation.

3.2. Prediction Performance

In the following section, the optimized estimators are benchmarked based on their estimation performance under varying initialization errors and the UDDS driving cycle.

EKF vs. UKF.

Under unbiased initialization ($\Delta SOC_0 = 0$, $\Delta C_{p,0} = 0$; Figure 3), the EKF and UKF tracked the true SOC closely. The steady–state errors fell in the 3% band over most of the drive cycle. This confirmed that both filters were well tuned for nominal starts.

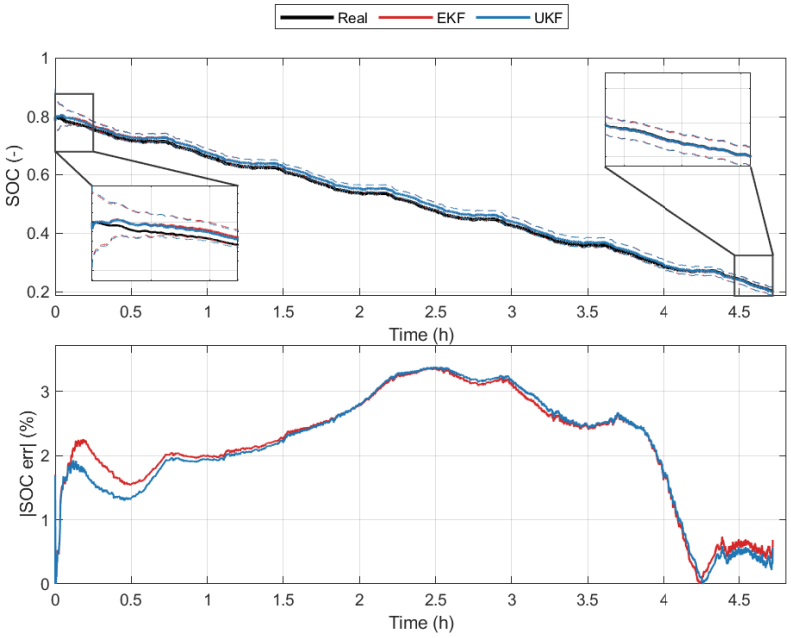


Figure 3. Comparison of EKF and UKF time series with initial SOC and capacity estimation error of 0%.

Under biased initialization (Figure 4), the EKF and UKF did not resolve the large capacity mismatch. The SOC estimates gradually diverged from the true value, and the mean bias gradually increased. This can be attributed to the unmodeled capacity error acting like an unobservable gain error. While the UKF showed slightly smoother transients, no qualitative advantage was seen once the initial capacity estimate was wrong.

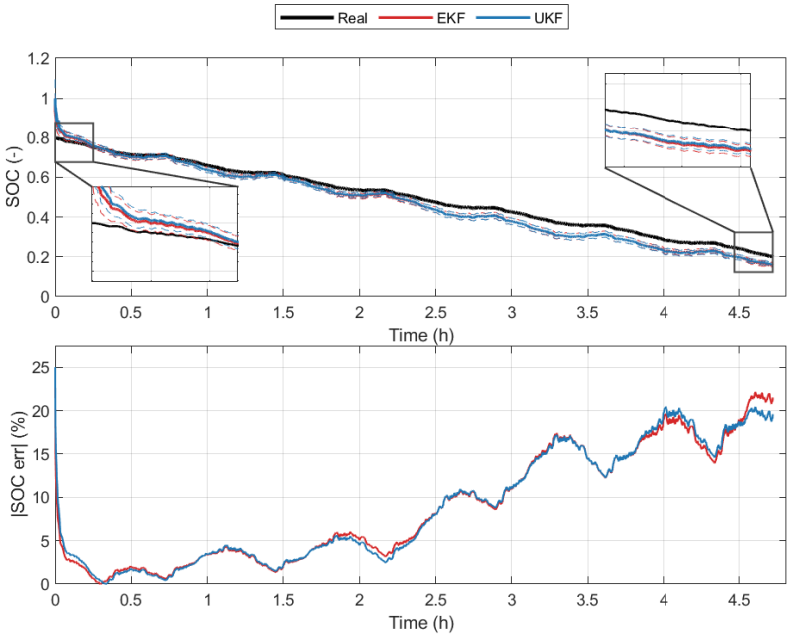


Figure 4. A comparison of EKF and UKF time series with an initial SOC estimation error of 20% and an initial capacity estimation error of −40%.

DEKF vs. DUKF.

With $\Delta SOC_0 = 0$, $\Delta C_{p,0} = 0$ (Figures 5 and 6), both dual estimators tracked the SOC changes smoothly and quickly converged for C_p and R_0.

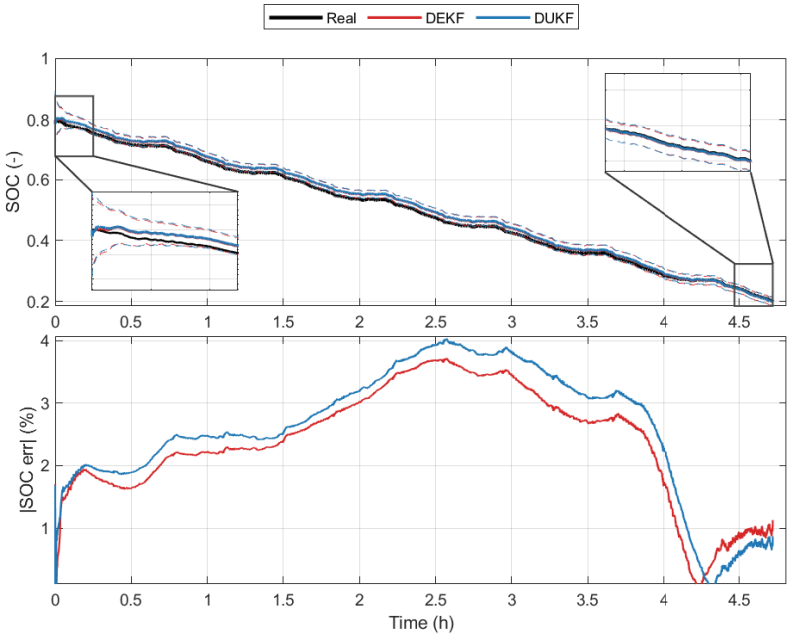


Figure 5. Comparison of DEKF and enhanced DUKF SOC time series with initial SOC and capacity estimation error of 0%.

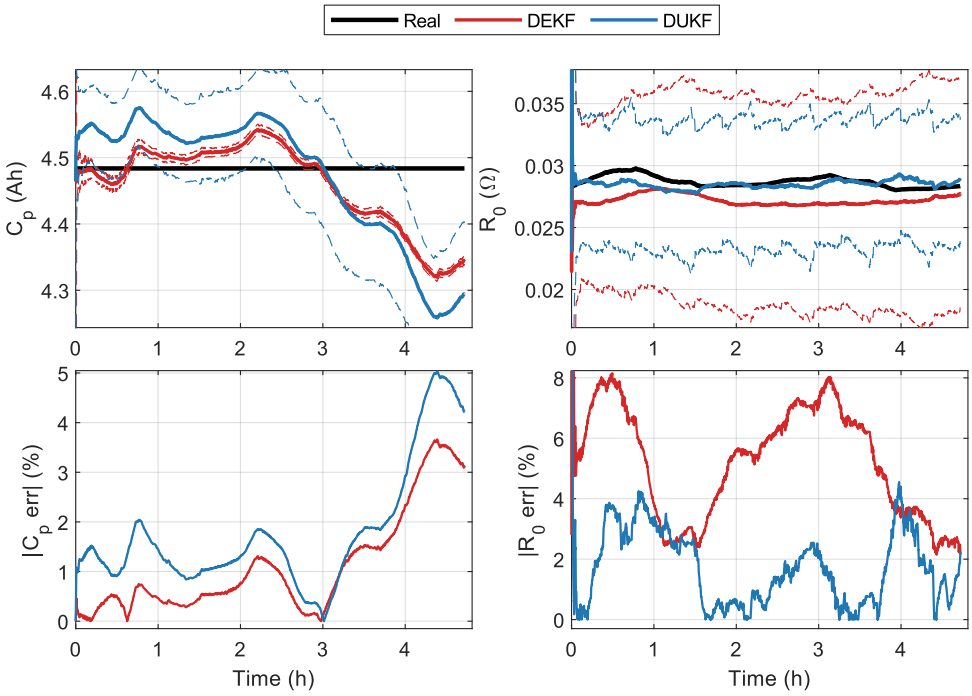


Figure 6. Comparison of DEKF and enhanced DUKF capacity and resistance time series with initial SOC and capacity estimation error of 0%.

With biased initialization (Figures 7 and 8), the key difference with respect to the single-state filters was evident, as both the DEKF and DUKF actively corrected the wrong capacity estimate. SOC transients were visible early in the cycle but quickly converged and tracked the true value. The capacity estimate $\widehat{C}_p$ moved toward the true value, and R_0 was tracked within a bounded range after a short settling phase. Between the two, the DUKF exhibited a faster, smoother convergence of $\widehat{C}_p$ and R_0, at the cost of higher computational load.

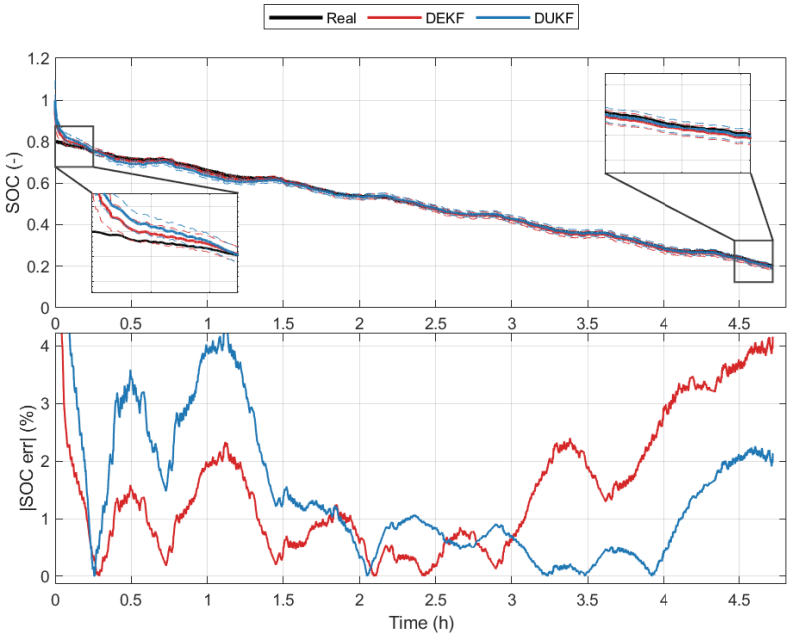


Figure 7. A comparison of DEKF and enhanced DUKF SOC time series with an initial SOC estimation error of 20% and an initial capacity estimation error of −40%.

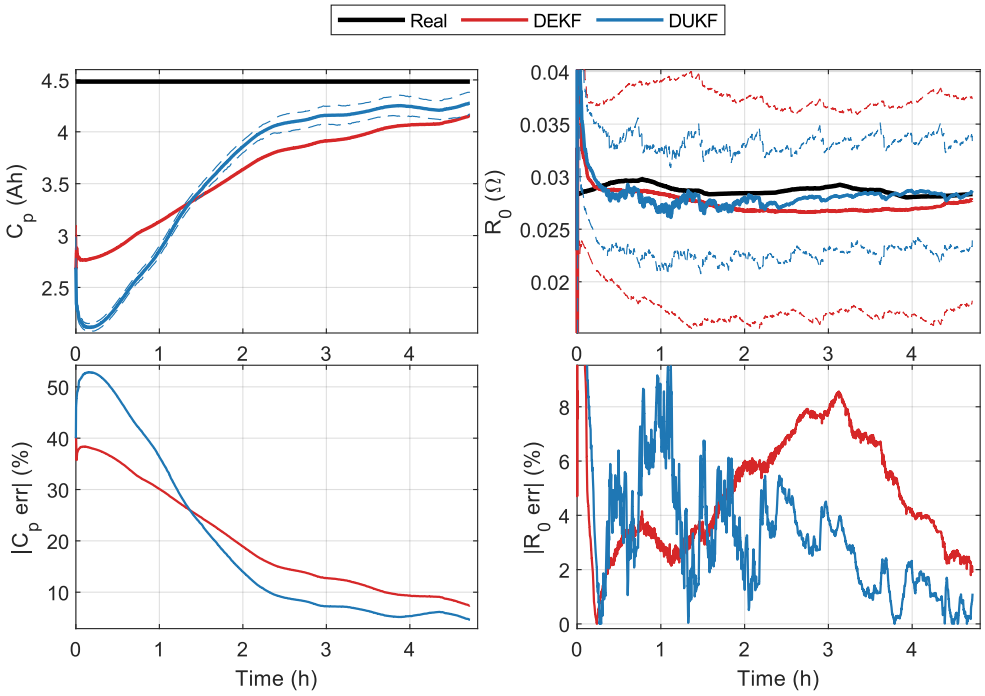


Figure 8. A comparison of DEKF and enhanced DUKF capacity and resistance time series with an initial SOC estimation error of 20% and an initial capacity estimation error of −40%.

3.3. RMSE Tables

The tables report the root-mean-square error (RMSE) for SOC capacity C_p across three initial SOC estimation errors $\Delta SOC_0 \in \{-0.20, 0, +0.20\}$ and three initial capacity estimation errors $\Delta C_{p,0} \in \{-0.40, 0, +0.40\}$.

Single-state filters.

When the initial capacity estimate was correct ($\Delta C_{p,0} = 0$), both the EKF and UKF reached a low SOC RMSE (about 1.7–2.1%), with only minor differences between them. As soon as the initial capacity was biased, the SOC RMSE increased significantly by roughly 31% for $\Delta C_{p,0} = -0.40$ and 20% for $\Delta C_{p,0} = +0.40$, while changing ΔSOC_0 from −0.20 to +0.20 only affected these numbers slightly.

For C_p, both the EKF and UKF did not correct the capacity bias, and the C_p RMSE was essentially 0% when $\Delta C_{p,0} = 0$ and about 40% when $|\Delta C_{p,0}| = 0.40$, regardless of ΔSOC_0. In short, the EKF and UKF behaved very similarly under these conditions, and neither reduced the estimation error of C_p. The SOC error RMSE for all tests on the single-state filters is reported in Table 3.

Table 3. SOC RMSE (%) for EKF and UKF. Rows: initial capacity error $\Delta C_{p,0}$; columns: initial SOC error ΔSOC_0.

	SOC RMSE (%)					
	EKF			**UKF**		
$\Delta C_{p,0}$	**−0.20**	**0.00**	**+0.20**	**−0.20**	**0.00**	**+0.20**
−0.40	31.0840	31.1870	31.3740	31.2820	31.3550	31.5740
0.00	1.9036	1.6768	2.0528	1.8372	1.6852	2.1309
+0.40	19.7600	19.9480	20.2570	19.7270	19.8980	20.3850

Dual-state filters.

Across all initialization scenarios, both dual estimators maintained a low SOC error. The DEKF yielded an SOC RMSE in the range 1.8–3.8%, whereas the DUKF achieved a narrower and lower range of 1.9–2.5% with reduced dependence on the initial offsets.

For capacity C_p, both dual estimators mitigated the impact of initial capacity estimation error. When $\Delta C_{p,0} = 0$, the DEKF produced a C_p RMSE in the range of 6–17% (lowest at $\Delta \mathrm{SOC}_0 = 0$), while that of the DUKF was lower at 4–10%. Under large initial capacity errors, $\Delta C_{p,0} = \pm 0.40$, the DEKF reduced the capacity RMSE to approximately 14–24%, and that of the DUKF remained lower at approximately 13–18%.

Overall, the DUKF achieved a lower RMSE in nearly all cases—both for the SOC and C_p—and showed greater consistency across initial offsets, whereas the DEKF exhibited higher sensitivity.

In addition to the SOC and capacity, both dual filters accurately tracked ohmic resistance R_0. Across all initialization scenarios, the average R_0 RMSE remained below 5% for both the DEKF and DUKF, with the latter showing smoother convergence and lower steady-state bias. The SOC and capacity error RMSE for all tests on the dual filters is reported in Table 4.

Table 4. The DEKF and DUKF RMSE (%). Rows are the initial capacity error; columns are the initial SOC error. Top: SOC RMSE. Bottom: C_p RMSE.

***SOC* RMSE (%)**						
	DEKF			**DUKF**		
$\Delta C_{p,0}$	-0.20	0.00	$+0.20$	-0.20	0.00	$+0.20$
-0.40	2.0410	1.8105	3.7857	1.9694	1.9184	2.2494
0.00	2.6388	2.1790	3.1055	2.0818	1.9689	2.2107
$+0.40$	3.2620	2.8447	3.0623	2.4441	2.2984	2.4511
C_p RMSE (%)						
	DEKF			**DUKF**		
$\Delta C_{p,0}$	-0.20	0.00	$+0.20$	-0.20	0.00	$+0.20$
-0.40	13.8910	19.9290	23.6310	12.8780	14.9000	17.6660
0.00	7.1080	6.3414	17.1010	4.2895	5.4480	9.5866
$+0.40$	24.3620	14.7730	14.7900	16.7670	12.9900	8.5820

As reported in Table 5, the UKF-based variants result in roughly 4.9 times higher computation cost per step compared to the EKF-based variants. This is due to sigma-point propagation, with the DUKF in particular being the most computationally demanding, consistent with its stronger precision and robustness reported above. Given a typical sampling period of 100 ms in production battery management systems, all filters, including the DUKF, operate comfortably within real-time constraints.

Table 5. Average per step execution time across all cycles and initialization scenarios. Values are computed as total runtime divided by number of time steps in each cycle and then averaged over cycles.

	EKF	**UKF**	**DEKF**	**DUKF**
Average per step time (µs)	6.8954	33.4990	8.5758	42.7640

In conclusion, the EKF and UKF estimators were accurate and efficient when the total capacity estimate was initialized close to the truth, as SOC accuracy degraded severely in

the presence of large errors. On the other hand, the DEKF and DUKF estimators maintained a low SOC and C_p RMSE by actively correcting C_p. The DUKF provided the best overall accuracy and convergence smoothness among the tested filters, at the cost of a higher computational load.

3.4. Enhancements to the Prediction Methodology

Two distinct challenges had to be addressed to develop a dual unscented estimation framework that was both numerically stable during operation and optimization and capable of tracking gradual battery aging:

1. The risk of losing the positive definiteness of the UKF estimation covariance.
2. The inherently weak sensitivity of the measured terminal voltage to total capacity C_p.

The measures introduced to address each issue are summarized below.

3.4.1. Robust Sigma-Point Generation in the UKF

When the state estimation covariance $P_{k|k-1}$ grew large, the Cholesky factorization, which was used to generate sigma-points, occasionally failed, producing `NaN` values and halting the filter estimation. This was attributed to two main reasons. First, large a priori covariance can push some sigma-points outside the physically admissible domain, such as forcing SOC beyond the $[0, 1]$ interval or making R_{ohm} negative, thereby invalidating later model evaluations. Second, the Cholesky factorization is numerically fragile, and with a covariance $P_{k|k-1}$ that is only positive semi-definite, even minor round-off errors can violate the strict definiteness required by Cholesky, causing the decomposition and the filter to abort.

Two complementary modifications were introduced to guarantee stable sigma-point generation. The first was a *physics-based clipping strategy*: whenever the raw sigma-points were derived, any component that lay outside its physically admissible range was projected back onto that range, for example,

$$\text{SOC}^{(i)} = \min\big(1, \max(0, \text{SOC}^{(i)})\big), \qquad R_{\text{ohm}}^{(i)}, C_{\text{dl}}^{(i)} > 0.$$

By preventing the filter from propagating impossible battery states, the procedure kept the a priori covariance $P_{k|k-1}$ well-conditioned and reduced the likelihood of failure of the subsequent square-root factorization. The second modification replaced the Cholesky factorization with a singular-value decomposition, $P = U\Sigma U^\top$, and employed $S = U\Sigma^{1/2}$ as the square root, as the SVD remained valid even when $P_{k|k-1}$ was merely positive *semi*-definite.

3.4.2. Enhancing Capacity Observability

The terminal voltage depends on capacity C_p only indirectly through the SOC based on the measurement equation (Equation (2)):

$$y_k = U_{\text{OCV}}(\text{SOC}_k) - U_{\text{RC1},k} - U_{\text{RC2},k} - R_0 i_k$$

To quantify how weak this dependency is, the dimensionless relative sensitivity is defined as

$$S_{y_k}^{C_p} = \frac{C_p}{y_k} \frac{\mathrm{d}y_k}{\mathrm{d}C_p} \tag{40}$$

Because the ohmic and RC voltage terms are independent of C_p, only the OCV term contributes:

$$\frac{\mathrm{d}\,U_{\mathrm{OCV}}(\mathrm{SOC}_k)}{\mathrm{d}C_p} = \frac{\partial\,U_{\mathrm{OCV}}(\mathrm{SOC}_k)}{\partial \mathrm{SOC}_k}\,\frac{\mathrm{dSOC}_k}{\mathrm{d}C_p}, \tag{41}$$

$$\frac{\mathrm{dSOC}_k}{\mathrm{d}C_p} = \frac{\mathrm{d}SOC_{k-1}}{\mathrm{d}C_p} + \frac{\eta_{k-1}\,i_{k-1}\,\Delta t}{{C_p}^2}. \tag{42}$$

Equation (42) reveals that the incremental contribution to $\mathrm{dSOC}_k/\mathrm{d}C_p$ is *quadratic* in the inverse of capacity. Substituting (41) and (42) into (40) therefore yields

$$S_{y_k}^{C_p} \propto \underbrace{\frac{1}{C_p}\,\frac{\partial\,U_{\mathrm{OCV}}(\mathrm{SOC}_k)}{\partial \mathrm{SOC}_k}}_{\text{dominant term}} + \mathcal{O}\left({C_p}^{-2}\right).$$

Because $\frac{\partial\,U_{\mathrm{OCV}}(\mathrm{SOC})}{\partial \mathrm{SOC}}$ is typically small (except for very high and low SOC), voltage-based SOH observability degrades under low-current or mild cycles, as sensitivity might become smaller than the sensor noise. In such regimes, the dual filters prioritize SOC accuracy, while SOH updates proceed slowly; convergence accelerates once segments with larger SOC swings appear. This is a fundamental limitation of voltage-only estimators. Consequently, voltage measurements only cannot reliably discriminate an error in C_p during normal driving unless exceptionally large SOC swings are observed.

To mitigate the poor observability of capacity C_p while preserving real-time execution, synthetic SOC–capacity coupling was implemented. This relationship is motivated by the inherent correlation between changes in the estimated total capacity and variations in the SOC, where an increase in capacity results in a smaller SOC drop per time step, as indicated by Equation (2). Before each UKF measurement update, the change in capacity in each parameter sigma-point $\chi_\theta^{(i)}$ was mapped onto an adjusted state of charge, which was utilized to estimate the OCV in the measurement function, thereby amplifying the influence of C_p on the predicted terminal voltage. Since the SOC–capacity correlation is not direct, a smoothing factor α was introduced to adjust the strength of this coupling.

$$SOC^{(i,\theta)} = SOC_{k+1}\,\frac{\chi_\theta^{(i)} + \alpha\hat{C}_{p_k}}{(1+\alpha)\hat{C}_{p_k}}$$

This formulation yields

$$\frac{\partial\,OCV\left(SOC^{(i,\theta)}\right)}{\partial\chi_\theta^{(i)}} \propto \frac{1}{1+\alpha}\,\frac{SOC_{k+1}}{\hat{C}_{p,k}}, \tag{43}$$

indicating that the observability gain for C_p decreases with increasing α. A parametric analysis across standard drive cycles under different initial estimation errors was performed, and it was confirmed that $\alpha = 0$ resulted in the lowest average estimation error for both capacity and SOC without significantly compromising numerical stability. The results are summarized in Table 6.

Table 6. The effect of the smoothing factor α on the average RMSE of SOC and capacity estimates in the DUKF.

	$\alpha = 0$	$\alpha = 10$	$\alpha = 20$	$\alpha = 40$	$\alpha = 80$
DUKF *SOC* RMSE (%)	2.1769	2.4443	2.4588	2.4799	2.6154
DUKF C_p RMSE (%)	11.456	12.365	12.736	13.151	14.039

The synthetic SOC–capacity coupling offered two principal advantages: it enhanced measurement sensitivity to capacity variations and was simple and lightweight to implement in existing code. However, several drawbacks remained. Firstly, estimation was still ineffective when the voltage measurement error became small. Secondly, because the coupling was artificial, it did not follow a physics-based model fully and could introduce modeling inconsistencies. Thirdly, the added gain could trigger overshoot or even instability in the capacity estimate if not tuned correctly. Finally, the fundamental SOC–capacity coupling problem remained, as the accurate estimation of the states could compromise the performance of the parameter estimator.

To assess the contribution of the proposed enhancement, the two representative scenarios utilized in the previous section were used for benchmarking the effect of disabling the enhancement for the DUKF while keeping the rest of the setup unchanged. The zero-bias case with $\Delta\text{SOC}_0 = 0$ and $\Delta C_{p,0} = 0$ (Figures 9 and 10) and the biased case with $\Delta\text{SOC}_0 = +0.20$ and $\Delta C_{p,0} = -0.40$ (Figures 11 and 12) were analyzed.

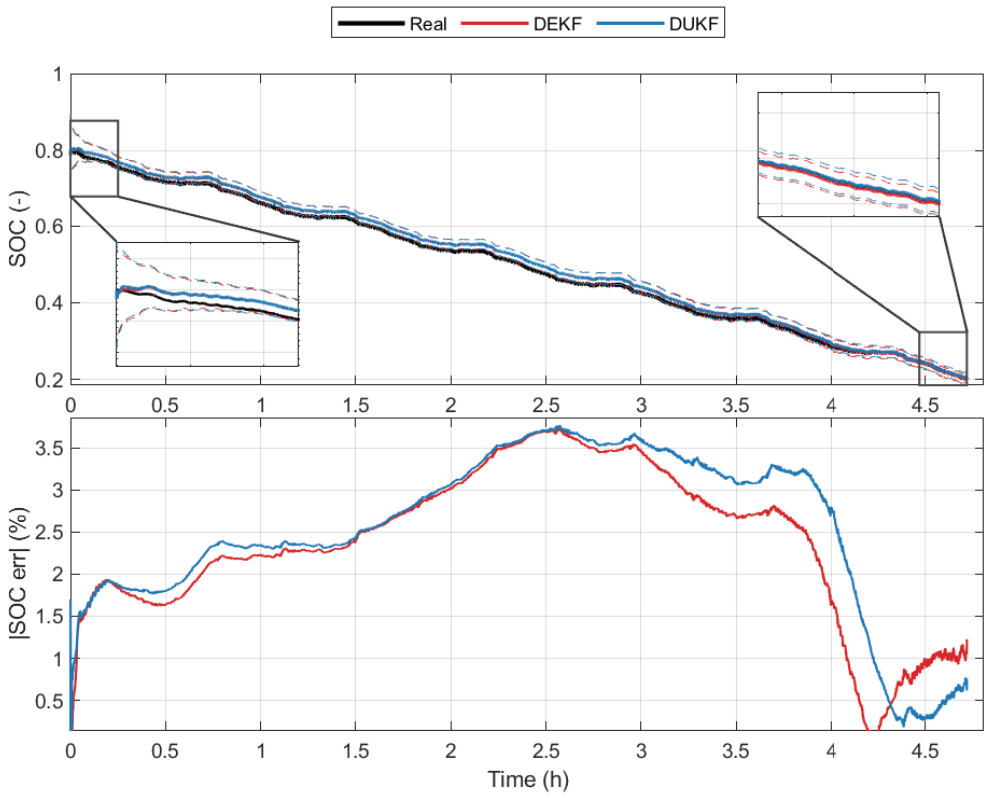


Figure 9. Comparison of DEKF and standard DUKF SOC time series with initial SOC and capacity estimation error of 0%.

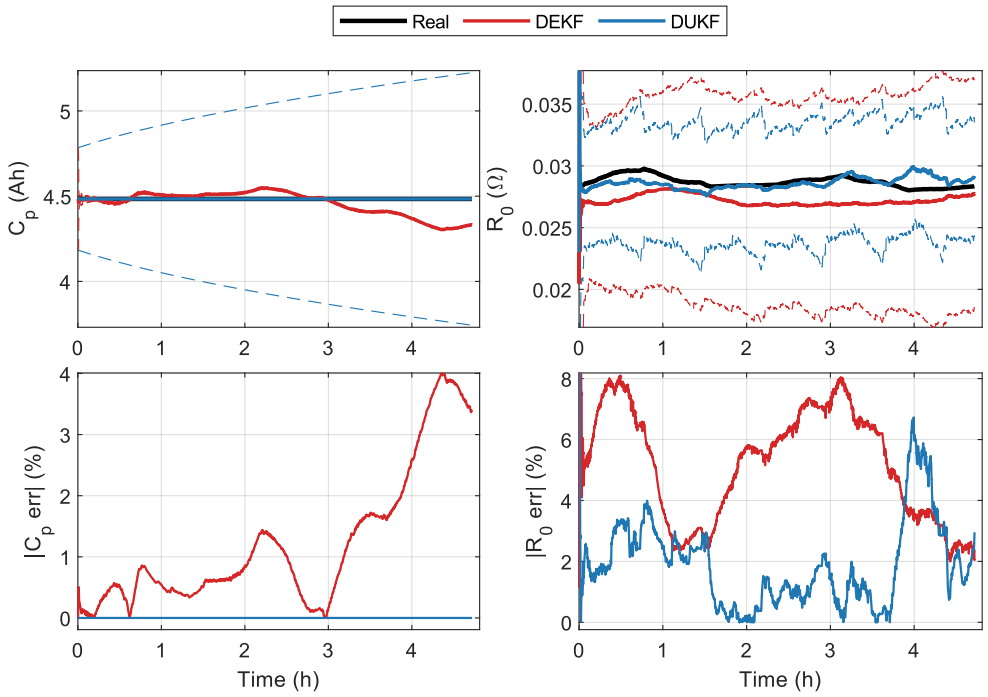


Figure 10. Comparison of DEKF and standard DUKF capacity and resistance time series with initial SOC and capacity estimation error of 0%.

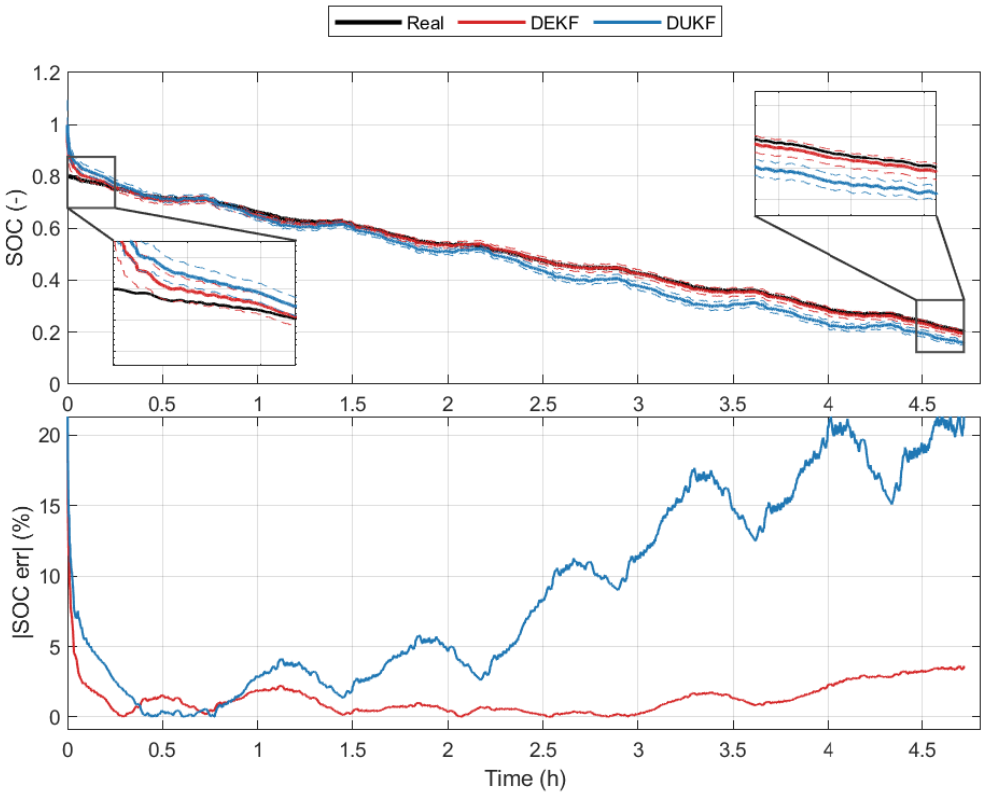


Figure 11. Comparison of DEKF and standard DUKF SOC time series with initial SOC estimation error of 20% and initial capacity estimation error of −40%.

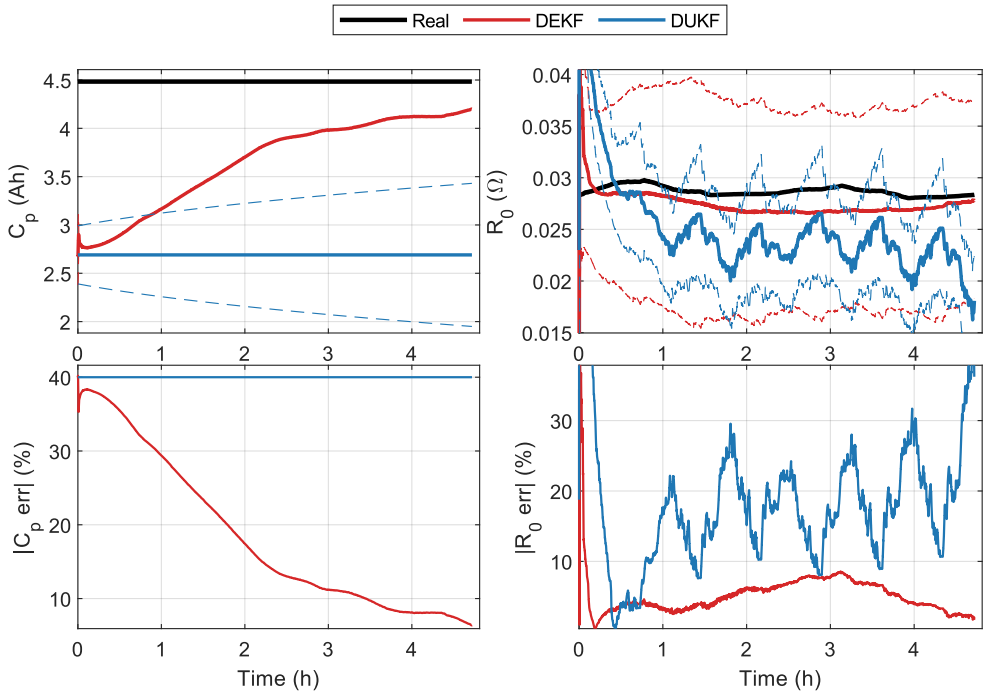


Figure 12. Comparison of DEKF and standard DUKF capacity and resistance time series with initial SOC estimation error of 20% and initial capacity estimation error of −40%.

Zero-Bias Case

Without enhancement, the DUKF showed a longer SOC transient compared to the enhanced version. The capacity estimate C_p converged slowly and retained a small steady error. The R_0 trajectory was also less stable, with larger variations before settling.

Biased Initial Conditions

With $\Delta\text{SOC}_0 = +0.20$ and $\Delta C_{p,0} = -0.40$, the DUKF *without* enhancement performed poorly, as the capacity estimate C_p updated very slowly and remained far from the true value over most of the cycle. The R_0 estimate was also inaccurate and highly variable, showing large swings. As a result, the SOC error continued to increase, primarily due to the persistent capacity bias. Overall, the non-enhanced DUKF performed significantly worse compared to the DEKF reference, whereas the enhanced DUKF handled the same offsets more effectively.

In conclusion, disabling enhancement consistently degraded DUKF performance by resulting in slower convergence and larger steady-state errors in both C_p and R_0 estimates. This confirmed that the enhancement was the main driver of the robustness observed in the time series comparisons and the RMSE tables of the DUKF estimator.

Finally, we note that this study was conducted at the cell level, which provides a controlled framework to evaluate estimator behavior without the confounding effects of thermal gradients or inter-cell imbalance. The proposed dual-filter framework establishes a solid foundation for future extensions toward pack-level implementations, where additional aspects such as temperature coupling, balancing strategies, and contact resistances can be systematically integrated and assessed.

4. Conclusions

This study compared the performance of single-state and dual-state Kalman filters for joint SOC and SOH estimation with covariances tuned by a structured, log-space, offline optimization. The results demonstrate the following findings.

Firstly, single-state filters provide accurate SOC estimation when the initial capacity estimate is correct, but they exhibit large SOC errors when the capacity is biased, since capacity acts as an unobservable gain (Table 3).

Dual filters effectively address this issue by adapting capacity online, which resulted in a sustained SOC RMSE near 2% across a wide range of initializations and reducing capacity estimation errors (Table 4). This is consistent with the findings in the prior literature on the sensitivity of SOC observers to capacity drift and on the benefits of dual estimation for aging compensation [3].

Among the investigated dual approaches, the DUKF achieved better SOC and capacity estimation compared to the DEKF (Figures 5–7). This improvement can be attributable to a better handling of model nonlinearities. Two implementation choices were essential in realizing this advantage. The first was numerically robust sigma-point generation combined with the physics-aware clipping of states and parameters to admissible domains with an SVD-based square-root factorization of the covariance. This prevented the loss of positive definiteness and avoided UKF breakdowns during aggressive adaptation and covariance optimization. Second, lightweight synthetic SOC–capacity coupling was introduced, which increased the effective measurement sensitivity to capacity, accelerating convergence and stabilizing. It was observed that disabling this coupling led to slower convergence and reduced DUKF performance under both unbiased and biased initializations (Figures 5–12).

It is important to note that optimizing the covariance parameters improved estimation performance across various driving cycles and initialization errors (Tables 1 and 2). Notably, the DUKF performed better with a comparatively larger Q^{θ} and R^{θ}, which regularized the stronger nonlinearity captured by sigma-points, which was observed in the smooth parameter trajectories. However, this came at the expense of computational cost, as sigma-point propagation and SVD updates increased the runtime relative to the DEKF by 490%, which could prove problematic for embedded battery management systems with tight CPU budgets.

This study considered two drive cycles and a lumped single-cell model without explicit hysteresis or temperature dependency; pack-level phenomena (cell imbalance, contact resistances) were omitted, only diagonal Q/R covariances were tuned, and the evaluation was based on simulations. To build on the findings, future work could (1) increase battery–model fidelity by introducing hysteresis and temperature effects; (2) implement adaptive Q and R updates during the estimation process; (3) introduce measurement noise into the estimation process; (4) integrate a machine learning model to enhance capacity–voltage sensitivity and benchmark it against synthetic coupling; and (5) validate the results in experimental settings.

Author Contributions: Conceptualization, F.M., A.S. and D.A.M.; methodology, F.M. and A.S.; software, A.S.; validation, F.M. and D.A.M.; formal analysis, A.S.; investigation, A.S.; resources, F.M.; data curation, A.S.; writing—original draft preparation, A.S. and F.M.; writing—review and editing, D.A.M.; visualization, A.S. and F.M.; supervision, F.M. and D.A.M.; project administration, F.M. and D.A.M. All authors have read and agreed to the published version of the manuscript.

Funding: This research received no external funding.

Data Availability Statement: The original contributions presented in this study are included in the article. Further inquiries can be directed to the corresponding authors.

Conflicts of Interest: The authors declare no conflicts of interest.

References

1. Lu, L.; Han, X.; Li, J.; Hua, J.; Ouyang, M. A review on the key issues for lithium-ion battery management in electric vehicles. *J. Power Sources* **2013**, *226*, 272–288. [CrossRef]
2. Hannan, M.A.; Lipu, M.S.; Hussain, A.; Mohamed, A. A review of lithium-ion battery state of charge estimation and management system in electric vehicle applications: Challenges and recommendations. *Renew. Sustain. Energy Rev.* **2017**, *78*, 834–854. [CrossRef]
3. Plett, G.L. *Battery Management Systems, Volume II: Equivalent-Circuit Methods*; Artech House Power Engineering Series; Artech House: Boston, MA, USA, 2016.
4. Xiong, R.; Li, L.; Tian, J. Towards a smarter battery management system: A critical review on battery state of health monitoring methods. *J. Power Sources* **2018**, *405*, 18–29. [CrossRef]
5. How, D.N.; Hannan, M.A.; Lipu, M.S.H.; Ker, P.J. State of Charge Estimation for Lithium-Ion Batteries Using Model-Based and Data-Driven Methods: A Review. *IEEE Access* **2019**, *7*, 136116–136136. [CrossRef]
6. Waag, W.; Fleischer, C.; Sauer, D.U. Critical review of the methods for monitoring of lithium-ion batteries in electric and hybrid vehicles. *J. Power Sources* **2014**, *258*, 321–339. [CrossRef]
7. Meng, J.; Ricco, M.; Luo, G.; Swierczynski, M.; Stroe, D.I.; Stroe, A.I.; Teodorescu, R. An Overview and Comparison of Online Implementable SOC Estimation Methods for Lithium-Ion Battery. *IEEE Trans. Ind. Appl.* **2018**, *54*, 1583–1591. [CrossRef]
8. Ng, K.S.; Moo, C.S.; Chen, Y.P.; Hsieh, Y.C. Enhanced coulomb counting method for estimating state-of-charge and state-of-health of lithium-ion batteries. *Appl. Energy* **2009**, *86*, 1506–1511. [CrossRef]
9. Lee, S.; Kim, J.; Lee, J.; Cho, B.H. State-of-charge and capacity estimation of lithium-ion battery using a new open-circuit voltage versus state-of-charge. *J. Power Sources* **2008**, *185*, 1367–1373. [CrossRef]
10. Weng, C.; Sun, J.; Peng, H. A unified open-circuit-voltage model of lithium-ion batteries for state-of-charge estimation and state-of-health monitoring. *J. Power Sources* **2014**, *258*, 228–237. [CrossRef]
11. Lavigne, L.; Sabatier, J.; Francisco, J.M.; Guillemard, F.; Noury, A. Lithium-ion Open Circuit Voltage (OCV) curve modelling and its ageing adjustment. *J. Power Sources* **2016**, *324*, 694–703. [CrossRef]
12. Yang, D.; Wang, Y.; Pan, R.; Chen, R.; Chen, Z. A Neural Network Based State-of-Health Estimation of Lithium-ion Battery in Electric Vehicles. *Energy Procedia* **2017**, *105*, 2059–2064. [CrossRef]
13. Yang, D.; Zhang, X.; Pan, R.; Wang, Y.; Chen, Z. A novel Gaussian process regression model for state-of-health estimation of lithium-ion battery using charging curve. *J. Power Sources* **2018**, *384*, 387–395. [CrossRef]
14. Yang, D.; Wang, Y.; Pan, R.; Chen, R.; Chen, Z. State-of-health estimation for the lithium-ion battery based on support vector regression. *Appl. Energy* **2018**, *227*, 273–283. [CrossRef]
15. Richardson, R.R.; Osborne, M.A.; Howey, D.A. Gaussian process regression for forecasting battery state of health. *J. Power Sources* **2017**, *357*, 209–219. [CrossRef]
16. You, G.W.; Park, S.; Oh, D. Diagnosis of Electric Vehicle Batteries Using Recurrent Neural Networks. *IEEE Trans. Ind. Electron.* **2017**, *64*, 4885–4893. [CrossRef]
17. Severson, K.A.; Attia, P.M.; Jin, N.; Perkins, N.; Jiang, B.; Yang, Z.; Chen, M.H.; Aykol, M.; Herring, P.K.; Fraggedakis, D.; et al. Data-driven prediction of battery cycle life before capacity degradation. *Nat. Energy* **2019**, *4*, 383–391. [CrossRef]
18. Acquarone, M.; Miretti, F.; Giuliacci, T.A.; Duque, J.; Misul, D.A.; Kollmeyer, P. Regression based battery state of health estimation for multiple electric vehicle fast charging protocols. *J. Power Sources* **2024**, *624*, 235601. [CrossRef]
19. Chen, L.; Bao, X.; Lopes, A.M.; Xu, C.; Wu, X.; Kong, H.; Ge, S.; Huang, J. State of health estimation of lithium-ion batteries based on equivalent circuit model and data-driven method. *J. Energy Storage* **2023**, *73*, 109195. [CrossRef]
20. Yang, H.; Hong, J.; Liang, F.; Xu, X. Machine learning-based state of health prediction for battery systems in real-world electric vehicles. *J. Energy Storage* **2023**, *66*, 107426. [CrossRef]
21. Lyu, Z.; Gao, R. A model-based and data-driven joint method for state-of-health estimation of lithium-ion battery in electric vehicles. *Int. J. Energy Res.* **2019**, *43*, 7956–7969. [CrossRef]
22. Bello, I.T.; Raza, H.; Michael, A.T.; Muneeswara, M.; Tewari, N.; Bingsen, W.; Cheung, Y.N.; Choi, Z.; Boles, S.T. Charging Ahead: The Evolution and Reliability of Nickel-Zinc Battery Solutions. *EcoMat* **2024**, *7*, e12505. [CrossRef]
23. Hu, X.; Li, S.; Peng, H. A comparative study of equivalent circuit models for Li-ion batteries. *J. Power Sources* **2012**, *198*, 359–367. [CrossRef]
24. Plett, G.L. Extended Kalman filtering for battery management systems of LiPB-based HEV battery packs - Part 3. State and parameter estimation. *J. Power Sources* **2004**, *134*, 277–292. [CrossRef]
25. He, H.; Xiong, R.; Zhang, X.; Sun, F.; Fan, J. State-of-charge estimation of the lithium-ion battery using an adaptive extended Kalman filter based on an improved Thevenin model. *IEEE Trans. Veh. Technol.* **2011**, *60*, 1461–1469. [CrossRef]
26. He, H.; Xiong, R.; Guo, H. Online estimation of model parameters and state-of-charge of LiFePO4 batteries in electric vehicles. *Appl. Energy* **2012**, *89*, 413–420. [CrossRef]

27. Ramadan, H.S.; Becherif, M.; Claude, F. Extended kalman filter for accurate state of charge estimation of lithium-based batteries: A comparative analysis. *Int. J. Hydrogen Energy* **2017**, *42*, 29033–29046. [CrossRef]
28. Plett, G.L. Sigma-point Kalman filtering for battery management systems of LiPB-based HEV battery packs. Part 2: Simultaneous state and parameter estimation. *J. Power Sources* **2006**, *161*, 1369–1384. [CrossRef]
29. Sun, F.; Hu, X.; Zou, Y.; Li, S. Adaptive unscented Kalman filtering for state of charge estimation of a lithium-ion battery for electric vehicles. *Energy* **2011**, *36*, 3531–3540. [CrossRef]
30. Tian, Y.; Xia, B.; Sun, W.; Xu, Z.; Zheng, W. A modified model based state of charge estimation of power lithium-ion batteries using unscented Kalman filter. *J. Power Sources* **2014**, *270*, 619–626. [CrossRef]
31. Wassiliadis, N.; Adermann, J.; Frericks, A.; Pak, M.; Reiter, C.; Lohmann, B.; Lienkamp, M. Revisiting the dual extended Kalman filter for battery state-of-charge and state-of-health estimation: A use-case life cycle analysis. *J. Energy Storage* **2018**, *19*, 73–87. [CrossRef]
32. Acquarone, M.; Miretti, F.; Misul, D.; Onori, S. *Sleek Dual Extended Kalman Filter for Battery State of Charge and State of Health Estimation in Electric Vehicle Applications*; SAE Technical Paper; SAE International: Warrendale, PA, USA, 2024. [CrossRef]
33. Andre, D.; Appel, C.; Soczka-Guth, T.; Sauer, D.U. Advanced mathematical methods of SOC and SOH estimation for lithium-ion batteries. *J. Power Sources* **2013**, *224*, 20–27. [CrossRef]
34. Wang, Q.; Kang, J.; Tan, Z.; Luo, M. An online method to simultaneously identify the parameters and estimate states for lithium ion batteries. *Electrochim. Acta* **2018**, *289*, 376–388. [CrossRef]
35. Kim, J.; Lee, S.; Cho, B.H. Complementary cooperation algorithm based on DEKF combined with pattern recognition for SOC/capacity estimation and SOH prediction. *IEEE Trans. Power Electron.* **2012**, *27*, 436–451. [CrossRef]
36. Fang, L.; Li, J.; Peng, B. Online estimation and error analysis of both SOC and SOH of lithium-ion battery based on DEKF method. *Energy Procedia* **2019**, *158*, 3008–3013. [CrossRef]
37. Hu, C.; Youn, B.D.; Chung, J. A multiscale framework with extended Kalman filter for lithium-ion battery SOC and capacity estimation. *Appl. Energy* **2012**, *92*, 694–704. [CrossRef]
38. Pozzato, G.; Allam, A.; Onori, S. Lithium-ion battery aging dataset based on electric vehicle real-driving profiles. *Data Brief* **2022**, *41*, 107995. [CrossRef]
39. Xu, L.; Cooper, J.; Allam, A.; Onori, S. Comparative Analysis of Numerical Methods for Lithium-Ion Battery Electrochemical Modeling. *J. Electrochem. Soc.* **2023**, *170*, 120525. [CrossRef]
40. Grano, E.; Villani, M.; de Carvalho Pinheiro, H.; Carello, M. Are We Testing Vehicles the Right Way? Challenges of Electrified and Connected Vehicles for Standard Drive Cycles and On-Road Testing. *World Electr. Veh. J.* **2025**, *16*, 94. [CrossRef]
41. Simon, D. *Optimal State Estimation: Kalman, H∞, and Nonlinear Approaches*; John Wiley & Sons, Inc.: Hoboken, NJ, USA, 2006. [CrossRef]
42. Waag, W.; Käbitz, S.; Sauer, D.U. Experimental investigation of the lithium-ion battery impedance characteristic at various conditions and aging states and its influence on the application. *Appl. Energy* **2013**, *102*, 885–897. [CrossRef]
43. Zhang, J.; Lee, J. A review on prognostics and health monitoring of Li-ion battery. *J. Power Sources* **2011**, *196*, 6007–6014. [CrossRef]
44. Kalman, R.E. A new approach to linear filtering and prediction problems. *J. Fluids Eng. Trans. ASME* **1960**, *82*, 35–45. [CrossRef]
45. Dalla Chiara, B.; Deflorio, F.; Eid, M. Analysis of real driving data to explore travelling needs in relation to hybrid–electric vehicle solutions. *Transp. Policy* **2019**, *80*, 97–116. [CrossRef]
46. Anselma, P.G.; Belingardi, G.; Falai, A.; Maino, C.; Miretti, F.; Misul, D.; Spessa, E. Comparing Parallel Hybrid Electric Vehicle Powertrains for Real-world Driving. In Proceedings of the 2019 AEIT International Conference of Electrical and Electronic Technologies for Automotive (AEIT AUTOMOTIVE), Turin, Italy, 2–4 July 2019; pp. 1–6. [CrossRef]

Disclaimer/Publisher's Note: The statements, opinions and data contained in all publications are solely those of the individual author(s) and contributor(s) and not of MDPI and/or the editor(s). MDPI and/or the editor(s) disclaim responsibility for any injury to people or property resulting from any ideas, methods, instructions or products referred to in the content.